DISCRETE AND CONTINUOUS
DYNAMICAL SYSTEMS
Volume **33**, Number **8**, August **2013**

doi:10.3934/dcds.2013.33.3671

pp. **3671–3705**

BRANCH INTERACTIONS AND LONG-TERM DYNAMICS FOR THE DIBLOCK COPOLYMER MODEL IN ONE DIMENSION

Ian Johnson

Department of Mathematical Sciences
George Mason University
Fairfax, VA 22030, USA

Evelyn Sander

Department of Mathematical Sciences
George Mason University
Fairfax, VA 22030, USA

Thomas Wanner

Department of Mathematical Sciences
George Mason University
Fairfax, VA 22030, USA

(Communicated by Hirokazu Ninomiya)

Abstract. Diblock copolymers are a class of materials formed by the reaction of two linear polymers. The different structures taken on by these polymers grant them special properties, which can prove useful in applications such as the development of new adhesives and asphalt additives. We consider a model for the formation of diblock copolymers first proposed by Ohta and Kawasaki [26]. Their model yields a Cahn-Hilliard-like equation, where a nonlocal term is added to the standard Cahn-Hilliard energy. We study the long-term dynamics of this model on one-dimensional domains through a combination of bifurcation theoretic results and numerical simulations. Our results shed light on how the complicated bifurcation behavior of the diblock copolymer model is related to the better known bifurcation structure of the Cahn-Hilliard equation. In addition, we demonstrate that this knowledge can be used to predict the long-term dynamics of solutions originating close to the homogeneous equilibrium. In particular, we show that the periodicity of the long-term limit of such solutions can be predicted by tracking certain secondary bifurcation points in the bifurcation diagram, and that the long-term limit is in general not given by the global energy minimizer.

1. **Introduction.** Diblock copolymers are formed by the chemical reaction of two linear polymers, or blocks, which contain different monomers. These blocks may often be thermodynamically incompatible, which means that following the reaction the blocks may be compelled to separate. However, following the reaction the blocks

---

2010 *Mathematics Subject Classification.* Primary: 35B40, 35K55, 65H20, 65M70; Secondary: 35B41, 74N15.

Key words and phrases. Cahn-Hilliard-Cook model, nucleation, stochastic partial differential equation, domain exit, large deviations, attractor structure.

are already covalently bonded. This means that it is not possible for them to separate on a macroscopic scale without adopting an entropically unfavorable extended configuration, in which the number of available states is severely limited relative to the native configuration. This conflict causes a phenomenon called *microphase separation*, where the two blocks separate on a mesoscopic scale. Microphase separation grants diblock copolymers the capacity for self-assembly into special geometries. These allow for the creation of materials with designer physical properties [3, 4, 9].

In the present paper, we consider the model for microphase separation in diblock copolymers described in [23], which in its original form was proposed by Ohta and Kawasaki [26] and Bahiana and Oono [2]. A derivation of this equation and the corresponding parameters is given in Choksi and Ren [7, 8]. On the domain Ω, the model defines the free-energy functional for the relative macroscopic monomer density u (i.e. the difference between the two monomer densities) by

$$E_{\lambda,\sigma}[u] = \int_\Omega \left(\frac{1}{2\lambda} |\nabla u|^2 + W(u) \right) dx + \frac{\sigma}{2} \int_\Omega \left| (-\triangle)^{-1/2} (u(x) - \mu) \right|^2 dx \qquad (1)$$

where $\mu = \int_\Omega u \, dx$ is the total mass of u, and W is a double-well potential with minima at ± 1. In the following, we always use the potential $W(u) = (u^2 - 1)^2/4$. The resulting evolution equation is then given by

$$\begin{aligned} u_t &= -\Delta \left(\Delta u + \lambda f(u) \right) - \lambda \sigma (u - \mu) \\ & \mu = \int_\Omega u(x) \, dx \\ & \frac{\partial u}{\partial n} = \frac{\partial \Delta u}{\partial n} = 0 \, , \quad x \in \partial\Omega \, , \end{aligned} \qquad (2)$$

where $f = -W'$ is the negative derivative of W, i.e., we have $f(u) = u - u^3$. The density function u is the locally averaged density of the two components across the domain, with the value 1 being interpreted as only component A being present at a point, and the value -1 being interpreted as only component B being present at a point. There are also three varying parameters, λ, σ, and μ, which have physical meanings. The parameters λ and σ are dimensionless functions of material parameters defined as follows:

$$\begin{aligned} \lambda &= \frac{3 \frac{N_A}{N} \left(1 - \frac{N_A}{N}\right) \chi |\Omega|^{2/3}}{l^2} \, , \\ \sigma &= \frac{36 |\Omega|^{2/3}}{\left(\frac{N_A}{N}\right)^2 \left(1 - \frac{N_A}{N}\right)^2 l^2 \chi N^2} \, , \end{aligned}$$

where N_A is the number of A units in the chain, N is the total length of the chain, χ is the Flory-Huggins interaction parameter describing the strength of the repulsion, $|\Omega|$ is the (physical) size of the domain, and l is the Kuhn statistical length which essentially measures typical distances between monomers. Informally, λ being large represents the short range repulsions being strong, inducing a strong compulsion to separate, while σ being large represents the long range chain elasticity forces being strong, inducing a strong compulsion to hold together. When $\sigma = 0$, this equation reduces to the standard Cahn-Hilliard equation.

In this paper, we focus our study on the one-dimensional domain $\Omega = (0,1)$, in which case the model reduces to

$$\begin{aligned} u_t &= -\left(u_{xx} + \lambda f(u)\right)_{xx} - \lambda\sigma(u-\mu) \\ &\mu = \int_0^1 u(x)\,dx \\ &u_x = u_{xxx} = 0\;, \quad x = 0,1\;, \end{aligned}$$

with $f(u) = u - u^3$. There are a number of previous treatments of this model showing the existence of a variety of solutions [16, 22, 25, 27, 28, 31] and using a combination of direct numerical simulations and analytical treatments [6, 7, 13, 17, 24, 32]. A closely related model for triblock copolymers has also been studied [18, 20, 29, 30, 33, 34].

Much of the previous theoretical work on the diblock copolymer model has concentrated on global minimizers of the energy functional $E_{\lambda,\sigma}$ described above. These studies have led to a wealth of results establishing the existence of global minimizing solutions on a variety of domains and in various dimensions. In addition, many results have described the geometry of the global minimizers in detail. Since our study is focused on the one-dimensional diblock copolymer model, we briefly mention one result due to Ren and Wei [28]. For the case $\mu = 0$, $\sigma > 0$, and $\Omega = (0,1)$, they show that the global minimizer of the diblock copolymer energy (1) is in general uniquely determined up to multiplication by -1, and is periodic with minimal period $P^{\lambda,\sigma}$ satisfying

$$P^{\lambda,\sigma} = \left(96\sqrt{2}\cdot\int_{-1}^{1}\sqrt{W(s)}\,ds\right)^{1/3}\cdot\left(\frac{1}{\lambda\sigma^2}\right)^{1/6} + O\left(\frac{1}{\lambda^{1/3}}\right) \qquad \text{for} \qquad \lambda\to\infty\;, \tag{3}$$

where $\int_{-1}^{1}\sqrt{W(s)}\,ds = 2/3$ for our nonlinearity. Thus, asymptotically for large integers $k \in \mathbb{N}$, the global energy minimizer has a wave number k (i.e., it is qualitatively like $\cos k\pi x$), or in other words, a minimal period of $2/k$, if the interaction parameters λ and σ satisfy

$$\sigma\sqrt{\lambda} \;\approx\; 96\sqrt{2}\cdot\frac{2}{3}\cdot\left(\frac{k}{2}\right)^3 \;=\; 8\sqrt{2}\cdot k^3\;. \tag{4}$$

Thus, for large values of λ the global minimizers of the diblock copolymer energy exhibit fine structure, i.e., periodicity with large wave number k. In addition, it was shown in [22] that in the limit $\lambda\to\infty$ the number of local minimizers of the energy functional $E_{\lambda,\sigma}$ converges to ∞. These results are in stark contrast to the Cahn-Hilliard case $\sigma = 0$. It is known [14] that the one-dimensional Cahn-Hilliard model has only two stable equilibrium solutions with exactly one transition layer each. One of these solutions is increasing, while the other one is decreasing.

The discussion of the last paragraph raises two natural questions. On the one hand, which mechanism introduces numerous stable solutions into the equilibrium structure of the diblock copolymer equation as σ is increased from zero? On the other hand, how do these changes affect the long-term dynamics of solutions to (2) which originate close to the unstable homogeneous equilibrium? In particular, while generic solutions of the Cahn-Hilliard model always converge to the global energy minimizer, can the same be said for the diblock copolymer model?

It is the goal of the present paper to shed light on the answers to these questions. In the course of this, we give rigorous bifurcation-theoretic results showing how intricate mode interactions lead to a wealth of secondary bifurcations in the equilibrium diagram for the diblock copolymer model, which in turn leads to numerous stable equilibrium solutions. Moreover, we demonstrate that the long-term behavior of solutions of (2) which originate close to the homogeneous equilibrium is in general not described by the global energy minimizer. Rather, generic solutions are trapped by a local minimizer which can be found by tracking certain secondary bifurcation points in the bifurcation diagram for the diblock copolymer equation.

The remainder of the paper is organized as follows. In Section 2 we present a rigorous local bifurcation analysis of mode interactions as the parameter σ is increased from zero. We show that these mode interactions occur at bifurcation points with two-dimensional kernels, and that the interaction types can be classified into three categories. The results of this section rigorously describe the bifurcation diagrams of the diblock copolymer model near the homogeneous state. In order to address the global bifurcation structure and the dynamical properties of the model, we turn to numerics. In Section 3 we describe our numerical methods for equilibrium continuation, spatial discretization, and direct simulation of the diblock copolymer model. In Section 4, we describe the results from our numerical simulations. Namely, the parameter space can be divided into regions with different dynamical behavior. We then use information from our bifurcation analysis to explain the transitions between these regions. In particular, we show that in general solutions of (2) which originate close to the homogeneous state will not reach the global energy minimizer. Finally, Section 5 contains a summary and discussion on the results of this paper.

2. Local bifurcation analysis.

As a first step towards uncovering the bifurcation structure of the one-dimensional diblock copolymer equation this section is devoted to giving a rigorous discussion of the local bifurcations which occur close to the constant equilibrium $u \equiv \mu$. Finding equilibrium solutions of the evolution equation is equivalent to solving the nonlinear operator equation

$$F(\lambda, \sigma, u) = -\Delta\left(\Delta u + \lambda f(u)\right) - \lambda\sigma(u - \mu) = 0 \,, \tag{5}$$

where we consider F as a parameter-dependent operator $F : \mathbb{R} \times \mathbb{R} \times X_\mu \to Y$, with Hölder type spaces

$$\begin{aligned} X_\mu &= \Big\{ u \in C^{4,\varrho}[0,1] \; : \; \int_0^1 u(x)\,dx = \mu \;\; \text{and} \\ &\qquad\qquad\qquad u_x(0) = u_{xxx}(0) = u_x(1) = u_{xxx}(1) = 0 \Big\} \,, \\ Y &= C^{0,\varrho}[0,1] \,, \end{aligned} \tag{6}$$

and with nonlinearity $f(u) = u - u^3$. Notice that for every choice of the parameters λ and σ the constant function $u \equiv \mu$ satisfies (5). In the following, we refer to this solution as the *trivial solution*. We completely describe the bifurcation diagram in the neighborhood of the trivial solution. For this, it is useful to employ the eigenvalues and eigenfunctions of the negative Laplacian $-\Delta$ on the one-dimensional domain $\Omega = (0,1)$ and subject to homogeneous Neumann boundary conditions. Recall that these are given by

$$\kappa_k = k^2\pi^2 \quad \text{and} \quad \varphi_k(x) = \sqrt{2}\cos k\pi x \quad \text{for} \quad k \in \mathbb{N} \,. \tag{7}$$

Note that since the space X_μ contains a mass constraint, the constant eigenfunction with eigenvalue zero will play no role in the following and has therefore been omitted. Using this notation, the following simple lemma explicitly determines the possible bifurcation points from the trivial solution of (5).

Lemma 1. *Using the above setting, bifurcations from the trivial solution $u \equiv \mu$ of the stationary diblock copolymer problem (5) can only occur at the λ-values*

$$\lambda(k, \sigma, \mu) = \frac{\kappa_k^2}{f'(\mu) \cdot \kappa_k - \sigma} \, , \tag{8}$$

where $\sigma \geq 0$. Since we are only interested in bifurcation points at positive λ-values, the indices k have to satisfy

$$\kappa_k > \frac{\sigma}{f'(\mu)} \, ,$$

and the total mass μ has to be in the spinodal region, i.e., we need to assume that $f'(\mu) > 0$.

Proof. The result is an immediate application of the implicit function theorem. For this, note that the Frechet derivative of F with respect to u is given by

$$D_u F(\lambda, \sigma, u)[v] = -\Delta \left(\Delta v + \lambda f'(u) v \right) - \lambda \sigma v \qquad \text{for} \qquad v \in X_0 \, .$$

One can readily see that for $u = \mu$ and $v = \varphi_k$ we have

$$D_u F(\lambda, \sigma, \mu)[\varphi_k] = \left(\lambda f'(\mu) \kappa_k - \kappa_k^2 - \lambda \sigma \right) \varphi_k \qquad \text{for} \qquad k \in \mathbb{N} \, .$$

Since the functions φ_k are complete in X_0, standard results show that the spectrum of $D_u F(\lambda, \sigma, \mu)$ consists only of the eigenvalues $\lambda f'(\mu) \kappa_k - \kappa_k^2 - \lambda \sigma$, where $k \in \mathbb{N}$. If all of these eigenvalues are nonzero, then $D_u F(\lambda, \sigma, \mu)$ is invertible with bounded inverse and the implicit function theorem rules out any bifurcation. Bifurcations can only occur when one of these eigenvalues is zero, and this is equivalent to (8). ☐

While the above result does provide a necessary condition for the location of the bifurcation points, it is not automatically guaranteed that bifurcations do occur at these points. For the special case of the Cahn-Hilliard equation, which corresponds to $\sigma = 0$, the potential bifurcation points are located at $\lambda = \kappa_k / f'(\mu) = k^2 \pi^2 / f'(\mu)$. It was shown in [14] that at each of these points a new solution branch bifurcates. These new branches do not contain any further bifurcation points themselves, and the k-th branch exists for all $\lambda > \kappa_k$.

In order to gain some first insight into what happens in the diblock copolymer case, we present a few numerically computed bifurcation diagrams in Figure 1 for the case of vanishing mass $\mu = 0$. In the top row of this figure, we present part of the bifurcation structure of the Cahn-Hilliard model, i.e., for $\sigma = 0$. In both panels, the horizontal axis represents λ in the interval $[0, 300]$. In the left panel, the vertical axis is the solution energy, while in the right panel the vertical axis is the L^2-norm of the solutions. In both panels, one can clearly see new solution branches emanating from the trivial solution curve $u \equiv 0$. Notice that each point on the bifurcating branches corresponds to two new solutions. For comparison, the second row in Figure 1 shows the numerically computed bifurcation diagram for the diblock copolymer model with $\sigma = 6$. While there still seem to be bifurcations occurring at all potential bifurcation points, the bifurcating branches exhibit considerably more complicated behavior that includes secondary bifurcation points. For the remainder of this section we provide a first theoretical insight into this behavior.

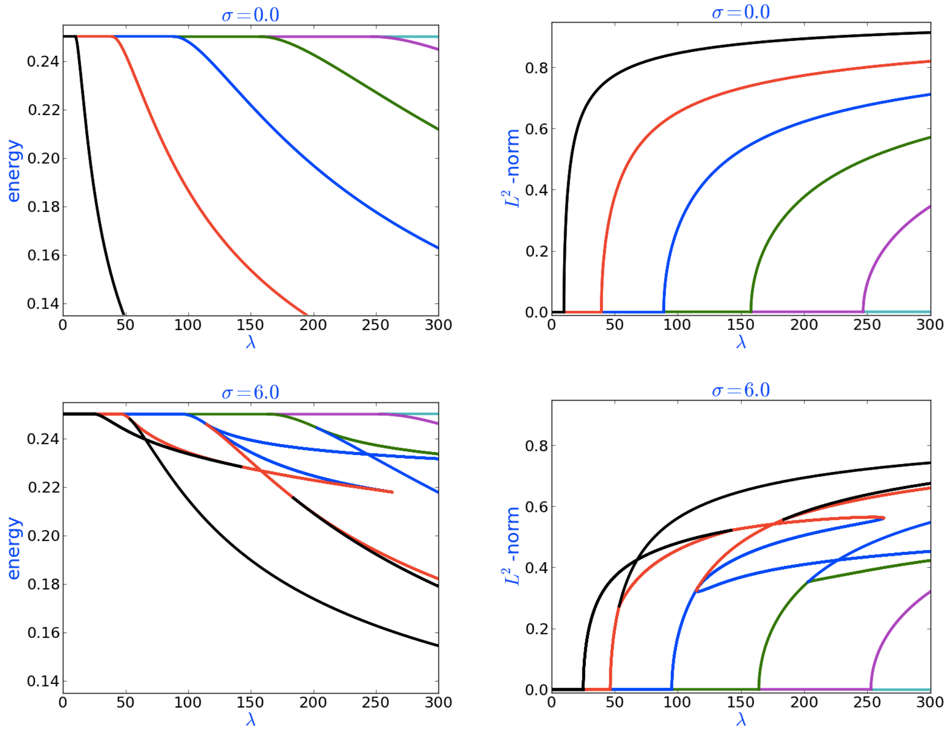

FIGURE 1. A few bifurcation diagrams. In each case the horizontal axis is λ. The panels in the top row are for the case $\sigma = \mu = 0$, i.e., for the classical Cahn-Hilliard case, while the panels in the second row are for $\sigma = 6$ and $\mu = 0$. In the left column, the vertical axis is given by the associated energy, while in the right column the L^2-norm of the stationary solutions are used.

It is not hard to see that if $u^* \neq 0$ denotes a nontrivial stationary solution for the classical Cahn-Hilliard equation for $\lambda = \lambda^*$ as well as $\sigma = 0$, then the point (λ^*, u^*) is a regular perturbation point with respect to perturbation in σ. In other words, as σ increases from 0, the bifurcation diagram of the Cahn-Hilliard model does not change qualitatively in a neighborhood of (λ^*, u^*). In view of the bifurcation diagrams shown in Figure 1, it is therefore natural to wonder how the complicated bifurcation diagram for $\sigma > 0$ arises from the one for $\sigma = 0$. For this, we take another look at the location (8) of possible bifurcation points derived in Lemma 1. We have already seen that for $\sigma = 0$ one obtains infinitely many bifurcation points $\lambda(k, 0) = \kappa_k$ for $k \in \mathbb{N}$. Now consider a fixed $k \in \mathbb{N}$. As σ increases from 0 towards $f'(\mu) \cdot \kappa_k > 0$, the location $\lambda(k, \sigma)$ of the bifurcation point increases monotonically from κ_k to $+\infty$. For $\sigma \geq f'(\mu) \cdot \kappa_k$ there is no longer a bifurcation point on the positive λ axis with kernel function φ_k. In other words, as we increase σ, the bifurcation points shown in the top row of Figure 1 move to the right and converge to $+\infty$ at finite values of σ. Since this motion is continuous with respect to σ, the branch corresponding to $k \in \mathbb{N}$ has to cross all branches for $\ell > k$.

In fact, one can show that

$$\lambda(k,\sigma,\mu) = \lambda(\ell,\sigma,\mu) \qquad \text{if and only if} \qquad \sigma = \frac{f'(\mu)}{\frac{1}{\kappa_k} + \frac{1}{\kappa_\ell}} = \frac{\kappa_k \kappa_\ell f'(\mu)}{\kappa_k + \kappa_\ell} \; . \tag{9}$$

This formula also shows that the following holds:

- The linearization $D_u F(\lambda,\sigma,\mu)$ of (5) has a two-dimensional kernel which is spanned by the functions φ_k and φ_ℓ if and only if $\lambda = \lambda(k,\sigma) = \lambda(\ell,\sigma)$ for some $k < \ell$, i.e., if (9) holds.
- The linearization $D_u F(\lambda,\sigma,\mu)$ of (5) has a one-dimensional kernel which is spanned by the function φ_k if and only if $\lambda = \lambda(k,\sigma)$ for some $k \in \mathbb{N}$, and if $\sigma \neq f'(\mu)\kappa_k\kappa_\ell/(\kappa_k + \kappa_\ell)$ for arbitrary $\ell \neq k$.
- For all other choices of λ and σ the linearization $D_u F(\lambda,\sigma,\mu)$ is invertible.

Thus, in order to understand the local bifurcation structure of (5), (6) close to the trivial solution $u \equiv \mu$, one only has to discuss the above-mentioned potential bifurcation points with one- or two-dimensional kernel. This is accomplished in the remainder of this section. For the sake of simplicity, we restrict our attention to the case $\mu = 0$, even though the general case can be treated analogously. We begin with the case of one-dimensional kernels.

Theorem 2.1 (One-Dimensional Kernel)**.** *Consider the nonlinear problem (5) for $u \in X_\mu$ as in (6), and assume that $\mu = 0$ and $f(u) = u - u^3$, i.e., we have $f'(\mu) = 1$. Furthermore, assume that*

$$\lambda^* = \lambda\left(k,\sigma^*\right) = \frac{\kappa_k^2}{\kappa_k - \sigma^*} \qquad \textit{for some} \qquad k \in \mathbb{N}$$

and that σ^* is such that (9) does not hold for any $\ell \in \mathbb{N}\backslash\{k\}$. Then the point $(\lambda, u) = (\lambda^*, 0)$ is a bifurcation point for the nonlinear problem

$$F(\lambda,\sigma^*,u) = 0 \qquad \textit{with} \qquad (\lambda,u) \in \mathbb{R}^+ \times X_0 \; ,$$

and there is exactly one branch of nontrivial solutions emanating from $(\lambda^*, 0)$. More precisely, there exists a smooth parameterization of the form $(\lambda(\alpha), u(\alpha))$ for the nontrivial solution branch, with α from a small interval around zero, which satisfies

$$\begin{aligned} \lambda(\alpha) &= \lambda^* + \frac{3\kappa_k^3}{2\left(\kappa_k - \sigma^*\right)^2} \cdot \alpha^2 + O\left(\alpha^3\right) \quad \textit{and} \\ u(\alpha) &= \alpha \cdot \varphi_k + O\left(\alpha^2\right) \; , \end{aligned}$$

as $\alpha \to 0$. In other words, the nontrivial solutions appear via a supercritical pitchfork bifurcation as λ increases through λ^*, and close to the bifurcation point the nontrivial solutions are qualitatively similar to $\varphi_k(x) = \sqrt{2}\cos k\pi x$.

Proof. This result follows from a standard application of the Crandall-Rabinowitz theorem as described in [35, Theorem 8.A]. □

Thus, at simple bifurcation points, i.e., at bifurcation points with one-dimensional kernel, the diblock copolymer model exhibits the bifurcation of one branch of nontrivial solutions. Moreover, one can easily show that the above result remains true for σ-values sufficiently close to σ^*, if the value of λ^* is adjusted appropriately.

We now turn our attention to the case of two-dimensional kernels. Since this involves understanding the interaction of two crossing branches, it is important to let the parameter σ vary as well. Recall that if we fix an integer $\ell \geq 2$, then the

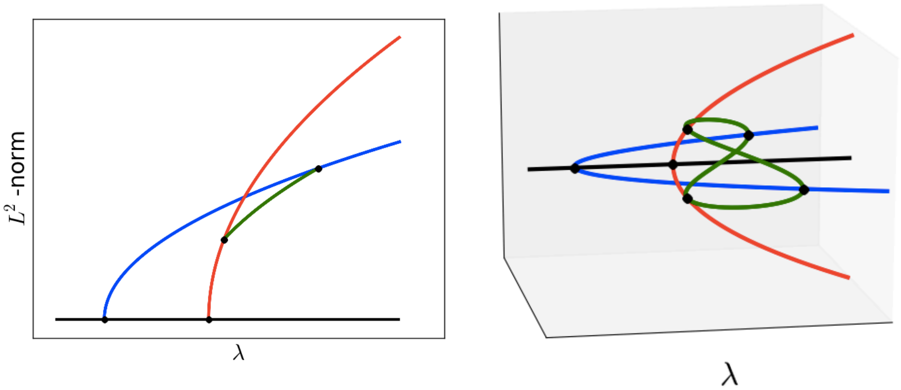

FIGURE 2. Local bifurcation structure for the case of a two-dimensional kernel with eigenfunctions φ_k and φ_ℓ, where $k < \ell/\sqrt{2}$ and $k \neq \ell/3$, for $\sigma < \sigma^*$. As σ increases towards σ^* the loop contracts and converges to the primary bifurcation point, and then disappears for $\sigma \geq \sigma^*$.

ℓ-branch, i.e., the nontrivial solution branch guaranteed by the previous theorem to originate from the bifurcation point $(\lambda, \sigma, u) = (\lambda(\ell, \sigma), \sigma, 0)$, will interact with the k-branches for all $1 \leq k < \ell$. Depending on the specific value of k there are three different interactions possible. These are the subject of the following three results.

Theorem 2.2 (Two-Dimensional Kernel of Type I)**.** *Consider the nonlinear elliptic problem (5) for $u \in X_\mu$ as in (6), and assume that $\mu = 0$ and $f(u) = u - u^3$, i.e., we have $f'(\mu) = 1$. Furthermore, assume that the parameters λ^* and σ^* are chosen in accordance with (9) in such a way that $\lambda^* = \lambda(k, \sigma^*) = \lambda(\ell, \sigma^*)$, for some integer k satisfying*

$$1 \leq k < \frac{\ell}{\sqrt{2}} \qquad \text{and} \qquad k \neq \frac{\ell}{3} \, .$$

Then the local bifurcation structure of (5) in a neighborhood of the point $(\lambda^*, \sigma^*, 0)$ can be described as follows.

- *For $\sigma < \sigma^*$ the k-branch originates to the left of the ℓ-branch with respect to λ. On each half of the ℓ-branch a secondary solution branch is generated through a supercritical pitchfork bifurcation, and these branches disappear in two subcritical pitchfork bifurcations on the two halves of the k-branch; see also Figure 2. In other words, the k- and the ℓ-branch are connected via a secondary loop of nontrivial solutions. As $\sigma \to \sigma^*$ from below, this loop contracts towards the bifurcation point $(\lambda^*, \sigma^*, 0)$.*
- *For $\sigma = \sigma^*$ there are exactly two nontrivial solution branches emanating from the bifurcation point $(\lambda^*, \sigma^*, 0)$, and these branches can locally be described as in Theorem 2.1.*
- *For $\sigma > \sigma^*$ the k-branch originates to the right of the ℓ-branch with respect to λ, and the two solution branches are no longer locally connected.*

More details on the convergence of the secondary bifurcation points as $\sigma \to \sigma^*$ from below can be found in the proof.

Proof. We consider the nonlinear problem

$$F(\lambda,\sigma,u) = -\Delta\left(\Delta u + \lambda f(u)\right) - \lambda\sigma u = 0 \qquad \text{with} \qquad u \in X_0 \;, \tag{10}$$

where the space X_0 was defined in (6). Standard results from nonlinear functional analysis show that the operator F is a Fredholm operator with index 0, i.e., the same is true for the Frechet derivative

$$Lv = D_u F(\lambda^*,\sigma^*,0)[v] = -\Delta\left(\Delta v + \lambda v\right) - \lambda\sigma v \;, \qquad L : X_0 \to Y \;,$$

where we have used the fact that $f'(0) = 1$. Based on our choice of λ^* and σ^*, the operator L has a two-dimensional nullspace which is given by

$$N(L) = \operatorname{span}\left[\varphi_k, \varphi_\ell\right] \;,$$

where φ_k and φ_ℓ were defined in (7). Using the methods described in [35, Section 8.4] one can easily show that we can decompose the spaces X_0 and Y in the form

$$X_0 = N(L) \oplus \widetilde{X}_0 \qquad \text{and} \qquad Y = \widetilde{Y} \oplus R(L) \;,$$

where $\widetilde{X}_0$ is the closed subspace of X_0 consisting of all functions whose L^2-inner products with both φ_k and φ_ℓ vanish. Moreover, we have $\widetilde{Y} = \operatorname{span}[\varphi_k, \varphi_\ell]$ and $R(L)$ consists of all functions in Y whose L^2-inner products with both φ_k and φ_ℓ vanish. Let $E : Y \to Y$ denote the projector with range $R(L)$ and kernel $\widetilde{Y}$, so that

$$E\varphi_k = E\varphi_\ell = 0 \;, \qquad \text{as well as} \qquad E\varphi_m = \varphi_m \quad \text{for all} \quad m \in \mathbb{N} \setminus \{k,\ell\} \;. \tag{11}$$

Finally, we represent functions $u \in X_0$ uniquely in the form

$$u = \alpha\varphi_k + \beta\varphi_\ell + w \in N(L) \oplus \widetilde{X}_0 \quad \text{for} \quad \alpha,\beta \in \mathbb{R} \quad \text{and} \quad w \in \widetilde{X}_0 \;.$$

Then the method of Lyapunov-Schmidt described in [35, Section 8.6] shows that the equation

$$EF\left(\lambda,\sigma,\alpha\varphi_k + \beta\varphi_\ell + W(\lambda,\sigma,\alpha,\beta)\right) = 0$$

uniquely determines a function $W(\lambda,\sigma,\alpha,\beta)$ which is defined in a neighborhood of $(\lambda^*,\sigma^*,0,0)$ and which takes values in $\widetilde{X}_0$. Moreover, the function W is smooth and one can show that all partial derivatives of W up to order two at the point $(\lambda^*,\sigma^*,0,0)$ vanish. Using this function W, solving the nonlinear problem (10) is then equivalent to solving the bifurcation equation

$$B(\lambda,\sigma,\alpha,\beta) = (I-E)F\left(\lambda,\sigma,\alpha\varphi_k + \beta\varphi_\ell + W(\lambda,\sigma,\alpha,\beta)\right) = 0 \;, \tag{12}$$

see [35, Section 8.6] for more details. Notice that $B : \mathbb{R}^4 \to \widetilde{Y} = \operatorname{span}[\varphi_k, \varphi_\ell]$, so solving the bifurcation equation amounts to solving a nonlinear system of two equations in the two unknowns α and β, and with two parameters λ and σ.

Since all functions involved in the definition of B in (12) are smooth, one can use a Taylor expansion to study the zeros of B close to the bifurcation point. Using standard techniques, and using the above knowledge on the derivatives of W up to order two, one can show that

$$
\begin{aligned}
D_{\alpha\lambda}B(\lambda^*,\sigma^*,0,0) &= (\kappa_k-\sigma^*)\,\varphi_k\ ,\\
D_{\beta\lambda}B(\lambda^*,\sigma^*,0,0) &= (\kappa_\ell-\sigma^*)\,\varphi_\ell\ ,\\
D_{\alpha\sigma}B(\lambda^*,\sigma^*,0,0) &= -\lambda^*\varphi_k\ ,\\
D_{\beta\sigma}B(\lambda^*,\sigma^*,0,0) &= -\lambda^*\varphi_\ell\ ,\\
D_{\alpha\lambda\sigma}B(\lambda^*,\sigma^*,0,0) &= -\varphi_k\ ,\\
D_{\beta\lambda\sigma}B(\lambda^*,\sigma^*,0,0) &= -\varphi_\ell\ ,\\
D_{\alpha\alpha\alpha}B(\lambda^*,\sigma^*,0,0) &= -9\lambda^*\kappa_k\varphi_k-3\lambda^*\kappa_{3k}(I-E)\varphi_{3k}\ , \qquad (13)\\
D_{\alpha\alpha\beta}B(\lambda^*,\sigma^*,0,0) &= -6\lambda^*\kappa_\ell\varphi_\ell-3\lambda^*\kappa_{|\ell-2k|}(I-E)\varphi_{|\ell-2k|}\ , \qquad (14)\\
D_{\alpha\beta\beta}B(\lambda^*,\sigma^*,0,0) &= -6\lambda^*\kappa_k\varphi_k\ ,\\
D_{\beta\beta\beta}B(\lambda^*,\sigma^*,0,0) &= -9\lambda^*\kappa_\ell\varphi_\ell\ ,
\end{aligned}
$$

and that all remaining derivatives of B of order at most three vanish at $(\lambda^*,\sigma^*,0,0)$. Note that there are two derivatives whose precise value depends on the choice of k and ℓ. In the present situation, we have assumed that $\ell\neq 3k$, which together with $k\neq 3k$ and (11) shows that the second term in (13) vanishes. Similarly, one can show that $|\ell-2k|\neq k$ as well as $|\ell-2k|\neq\ell$, and therefore also the second term in (14) vanishes. If we now project the equation $B(\lambda,\sigma,\alpha,\beta)=0$ onto the subspaces spanned by φ_k or φ_ℓ, and then multiply the resulting equations by $2/(3\lambda^*\kappa_k)$ or by $2/(3\lambda^*\kappa_\ell)$, respectively, and if we introduce the abbreviations

$$\nu=\lambda-\lambda^* \qquad \text{as well as} \qquad \eta=\sigma-\sigma^*\ ,$$

then the bifurcation equation (12) is equivalent to the two-dimensional system

$$
\begin{aligned}
0 &= \alpha\left(c_{11}\nu-c_{12}\nu\eta-c_{13}\eta-\alpha^2-2\beta^2\right)+R_\alpha(\alpha,\beta,\nu,\eta)\ , \qquad (15)\\
0 &= \beta\left(c_{21}\nu-c_{22}\nu\eta-c_{23}\eta-2\alpha^2-\beta^2\right)+R_\beta(\alpha,\beta,\nu,\eta)\ , \qquad (16)
\end{aligned}
$$

where we define

$$
\begin{aligned}
c_{11} &= \frac{2(\kappa_k-\sigma^*)}{3\lambda^*\kappa_k}\ , & c_{12} &= \frac{2}{3\lambda^*\kappa_k}\ , & c_{13} &= \frac{2}{3\kappa_k}\ ,\\
c_{21} &= \frac{2(\kappa_\ell-\sigma^*)}{3\lambda^*\kappa_\ell}\ , & c_{22} &= \frac{2}{3\lambda^*\kappa_\ell}\ , & c_{23} &= \frac{2}{3\kappa_\ell}\ ,
\end{aligned}
$$

and with

$$R_{\alpha/\beta}(\alpha,\beta,\nu,\eta)=|(\alpha,\beta)|\cdot O\left(|(\alpha,\beta,\nu,\eta)|^3\right)\ .$$

By employing scaling methods as in [19], one can easily see that solving the bifurcation equation can then be reduced to solving the above system to leading order, i.e., by ignoring the remainder terms $R_{\alpha/\beta}(\alpha,\beta,\nu,\eta)$. The actual solutions will differ from the ones of the reduced system only by higher-order terms.

One can readily see that in the case $\alpha=0$, the variable β can be determined by equating the expression in parentheses in (16) to zero, and that this in fact furnishes the k-branch from Theorem 2.1. Similarly, setting $\beta=0$ and determining the variable α in such a way that the expression in parentheses in (15) equals zero gives the ℓ-branch. Thus, nontrivial solution branches occur if the system

$$
\begin{aligned}
\alpha^2+2\beta^2 &= c_{11}\nu-c_{12}\nu\eta-c_{13}\eta\ , \qquad (17)\\
2\alpha^2+\beta^2 &= c_{21}\nu-c_{22}\nu\eta-c_{23}\eta \qquad (18)
\end{aligned}
$$

has nontrivial solutions. One can easily see that this system of equations only has a nontrivial solution if both right-hand sides are positive. Moreover, in this case the solution for each separate equation is given by an ellipse in the α-β-plane, where the ellipse in (17) is stretched vertically and the one in (18) is stretched horizontally. Since the expressions on the right-hand sides are different, these ellipses do not have to intersect. In fact, there exist nontrivial intersections if and only if

$$\frac{1}{2} \le \frac{c_{21}\nu - c_{22}\nu\eta - c_{23}\eta}{c_{11}\nu - c_{12}\nu\eta - c_{13}\eta} \le 2 \, . \tag{19}$$

If the fraction equals $1/2$, then the ellipses intersect in two points on the β-axis, if it equals 2 then they intersect in two points on the α-axis; values in between yield four nontrivial solutions away from the coordinate axes. Solving these two equalities for ν one obtains that

$$\nu = \nu_\ell^*(\eta) = -\frac{(c_{13} - 2c_{23})\eta}{(2c_{21} - c_{11}) + \eta(c_{12} - 2c_{22})} \quad \text{gives two solutions on the } \ell\text{-branch} \, , \tag{20}$$

while

$$\nu = \nu_k^*(\eta) = -\frac{(2c_{13} - c_{23})\eta}{(c_{21} - 2c_{11}) + \eta(2c_{12} - c_{22})} \quad \text{gives two solutions on the } k\text{-branch} \, , \tag{21}$$

as long as the right-hand sides in both (17) and (18) are strictly positive.

Using our assumptions on k and ℓ one can now verify that all the expressions in parentheses in both (20) and (21) are strictly positive, so for η close to 0 these identities yield ν-values close to 0 of the opposite sign. Furthermore, one can show the case $\eta > 0 > \nu$ leads to negative right-hand sides in both (17) and (18), i.e., to no nontrivial solutions. On the other hand, if $\eta < 0 < \nu$ satisfy (20) and (21), then we do in fact obtain nontrivial solutions. Finally, we have

$$\nu_\ell^*(\eta) < \nu_k^*(\eta) \quad \text{for} \quad \sigma < 0 \quad \text{close to zero} \ ,$$

and this guarantees the secondary loop described in the theorem for all $\eta < 0$ close to zero. In fact, the solutions on this loop are given by

$$\alpha = \pm\sqrt{\frac{2(c_{21}\nu - c_{22}\nu\eta - c_{23}\eta) - (c_{11}\nu - c_{12}\nu\eta - c_{13}\eta)}{3}} \, , \tag{22}$$

$$\beta = \pm\sqrt{\frac{2(c_{11}\nu - c_{12}\nu\eta - c_{13}\eta) - (c_{21}\nu - c_{22}\nu\eta - c_{23}\eta)}{3}} \, , \tag{23}$$

to leading order, for all $\sigma < 0$ close to zero and all $\nu_\ell^*(\eta) < \nu < \nu_k^*(\eta)$. This completes the proof of the theorem. ☐

The above theorem rigorously proves that in contrast to the case of the Cahn-Hilliard equation, the diblock copolymer model does indeed exhibit multiple nontrivial secondary solution branches. We now turn our attention to the exceptional case $k = \ell/3$ which had to be excluded above. This case is a resonance phenomenon which is due to the specific form of our nonlinearity $f(u) = u - u^3$, and can be described as follows.

Theorem 2.3 (Two-Dimensional Kernel of Type II). *Consider the nonlinear elliptic problem (5) for* $u \in X_\mu$ *as in (6), and assume that* $\mu = 0$ *and* $f(u) = u - u^3$*, i.e., we have* $f'(\mu) = 1$*. Furthermore, assume that the parameters* λ^* *and* σ^* *are*

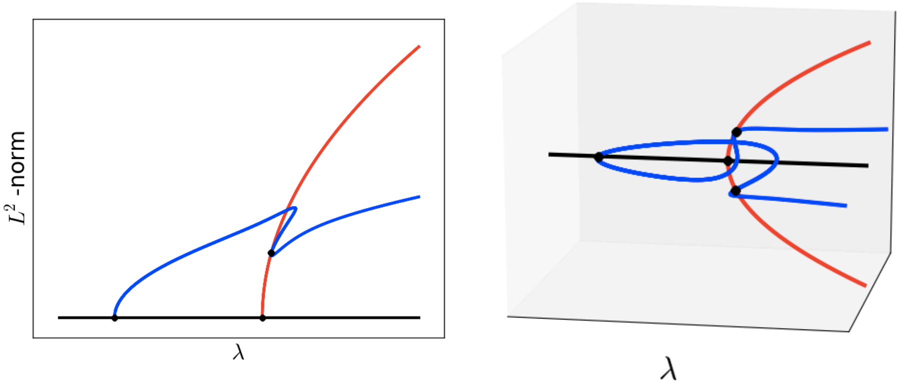

FIGURE 3. Local bifurcation structure for the case of a two-dimensional kernel with eigenfunctions φ_k and φ_ℓ, where $k = \ell/3$, for $\sigma < \sigma^*$. As σ increases towards σ^* the secondary bifurcation points on the red ℓ-branch converge to the primary bifurcation point. For $\sigma \geq \sigma^*$ the two branches are no longer connected locally.

chosen in accordance with (9) in such a way that $\lambda^* = \lambda(k, \sigma^*) = \lambda(\ell, \sigma^*)$*, for some integer* k *satisfying*

$$k = \frac{\ell}{3} \, .$$

Then the local bifurcation structure of (5) in a neighborhood of the point $(\lambda^*, \sigma^*, 0)$ *can be described as follows.*

- *For* $\sigma < \sigma^*$ *the* k*-branch originates to the left of the* ℓ*-branch with respect to* λ*. Each half of the* k*-branch intersects a half of the* ℓ*-branch via a supercritical pitchfork bifurcation as shown in Figure 3. In other words, the* k*- and the* ℓ*-branch are connected at two secondary bifurcation points. As* $\sigma \to \sigma^*$ *from below, these bifurcation points converge to the bifurcation point* $(\lambda^*, \sigma^*, 0)$*.*
- *For* $\sigma = \sigma^*$ *there are exactly two nontrivial solution branches emanating from the bifurcation point* $(\lambda^*, \sigma^*, 0)$*, and these branches can locally be described as in Theorem 2.1.*
- *For* $\sigma > \sigma^*$ *the* k*-branch originates to the right of the* ℓ*-branch with respect to* λ*, and the two solution branches are no longer locally connected.*

Proof. The proof of this result uses the same framework as the proof of the previous theorem. The changes in the bifurcation behavior are due to the last terms in equations (13) and (14). In the case $\ell = 3k$ these terms are nonzero, and this implies that the bifurcation equation (12) is now equivalent to the two-dimensional system

$$\begin{aligned} 0 &= \alpha \left(c_{11}\nu - c_{12}\nu\eta - c_{13}\eta - \alpha^2 - \alpha\beta - 2\beta^2 \right) + R_\alpha(\alpha, \beta, \nu, \eta) \, , \\ 0 &= \beta \left(c_{21}\nu - c_{22}\nu\eta - c_{23}\eta - 2\alpha^2 - \beta^2 \right) - \frac{\alpha^3}{3} + R_\beta(\alpha, \beta, \nu, \eta) \, , \end{aligned}$$

where the constants c_{ij} were defined in the context of (15) and (16), and we have

$$R_{\alpha/\beta}(\alpha, \beta, \nu, \eta) = |(\alpha, \beta)| \cdot O\left(|(\alpha, \beta, \nu, \eta)|^3 \right) \, .$$

Using a discussion similar to — but somewhat more tedious than — the one in the proof of Theorem 2.2 one can then establish the claimed bifurcation picture. ☐

Note that the above two results furnish complete descriptions for the interactions of the k- and the ℓ-branch for all $k < \ell/\sqrt{2}$. In particular, the secondary bifurcations in Figure 1 at $\sigma = 6.0$ are of Types I and II. The following final result of this section addresses the missing cases, i.e., we now consider $\ell/\sqrt{2} < k < \ell$.

Theorem 2.4 (Two-Dimensional Kernel of Type III)**.** *Consider the nonlinear elliptic problem (5) for $u \in X_\mu$ as in (6), and assume that $\mu = 0$ and $f(u) = u - u^3$, i.e., we have $f'(\mu) = 1$. Furthermore, assume that the parameters λ^* and σ^* are chosen in accordance with (9) in such a way that $\lambda^* = \lambda(k, \sigma^*) = \lambda(\ell, \sigma^*)$, for some integer k satisfying*

$$\frac{\ell}{\sqrt{2}} < k < \ell \, .$$

Then the local bifurcation structure of (5) in a neighborhood of the point $(\lambda^*, \sigma^*, 0)$ can be described as follows.

- *For $\sigma < \sigma^*$ the k-branch originates to the left of the ℓ-branch with respect to λ. Each half of the ℓ-branch undergoes a supercritical pitchfork bifurcation which leads to two additional branches of nontrivial solutions as shown in the top row of Figure 4. As $\sigma \to \sigma^*$ from below, the secondary bifurcation points converge to the bifurcation point $(\lambda^*, \sigma^*, 0)$.*
- *For $\sigma = \sigma^*$ there are exactly four nontrivial solution branches emanating from the bifurcation point $(\lambda^*, \sigma^*, 0)$. Two of these branches can locally be described as in Theorem 2.1, the remaining two are described in the proof below.*
- *For $\sigma > \sigma^*$ the k-branch originates to the right of the ℓ-branch with respect to λ. Each half of the k-branch undergoes a supercritical pitchfork bifurcation which leads to two additional branches of nontrivial solutions as shown in the bottom row of Figure 4. As σ increases beyond σ^*, the secondary bifurcation points move away from the bifurcation point $(\lambda^*, \sigma^*, 0)$.*

More details on the convergence of the secondary bifurcation points as $\sigma \to \sigma^*$ can be found in the proof.

Proof. The proof of this result uses exactly the same setting as the proof of Theorem 2.4. Under the present assumptions on k and ℓ the last terms in equations (13) and (14) vanish. Thus, the bifurcation equation (12) is equivalent to the two-dimensional system (15), (16) that was already discussed before, and we can again restrict our discussion to the leading order system (17), (18). In other words, for nontrivial solutions to exist we need both

$$c_{11}\nu - c_{12}\nu\eta - c_{13}\eta > 0 \quad \text{and} \quad c_{21}\nu - c_{22}\nu\eta - c_{23}\eta > 0 \, , \tag{24}$$

as well as

$$\frac{1}{2} \le \frac{c_{21}\nu - c_{22}\nu\eta - c_{23}\eta}{c_{11}\nu - c_{12}\nu\eta - c_{13}\eta} \le 2 \, . \tag{25}$$

The left inequality is satisfied as an equality if

$$\nu = \nu_\ell^*(\eta) = \frac{(2c_{23} - c_{13})\eta}{(2c_{21} - c_{11}) - \eta(2c_{22} - c_{12})} \, , \qquad \text{and furnishes two solutions on the } \ell\text{-branch} \, , \tag{26}$$

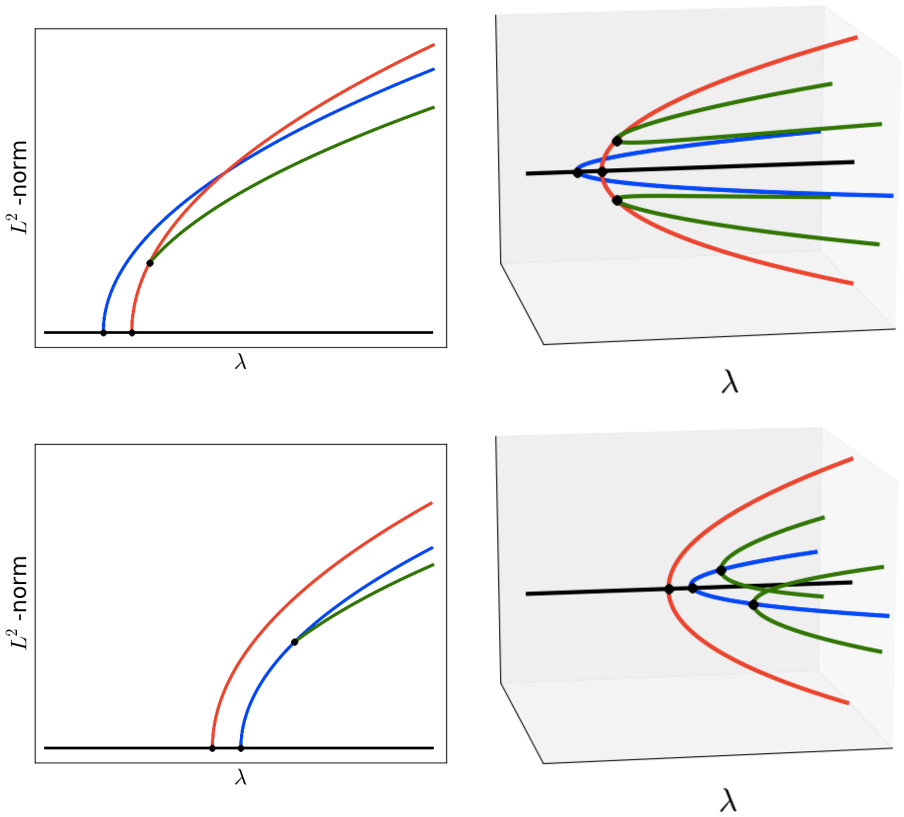

FIGURE 4. Local bifurcation structure for the case of a two-dimensional kernel with eigenfunctions φ_k and φ_ℓ, where $\ell/\sqrt{2} < k < \ell$. The top row corresponds to $\sigma < \sigma^*$, the bottom row to $\sigma > \sigma^*$. As σ increases towards σ^* from below, the secondary bifurcation points on the red ℓ-branch converge to the primary bifurcation point. For $\sigma > \sigma^*$ these two branches are now attached to the blue k-branch and the secondary bifurcation points on this branch move away from the primary bifurcation point.

while the right inequality is satisfied as an equality if

$$\nu = \nu_k^*(\eta) = \frac{(2c_{13} - c_{23})\eta}{(2c_{11} - c_{21}) - \eta(2c_{12} - c_{22})} \,, \qquad \text{and furnishes two solutions on the } k\text{-branch} \,. \tag{27}$$

Notice that while the formulas for $\nu_\ell^*(\eta)$ and $\nu_k^*(\eta)$ are the same as before, we rewrote them slightly for our current discussion. More precisely, the terms have been rearranged in such a way that all the expressions in parentheses in both (26) and (27) are strictly positive.

As in the proof of Theorem 2.2 one can show that for η close to 0 these identities yield ν-values close to 0, which now are of the same sign as η. In order to satisfy the positivity requirement in (24) and the inequalities in (25) one has to have $\eta < 0$ and $\nu_\ell^*(\eta) \le \nu$, or $\eta > 0$ and $\nu_k^*(\eta) \le \nu$. The first of these inequalities corresponds to the secondary supercritical branches on the ℓ-branch, while the second inequality

Branch Interactions at Two-Dimensional Kernels			
k-Range	Interaction	Figure	Description
$1 \leq k < \dfrac{\ell}{3}$	Type I	2	A secondary loop which connects the k- and the ℓ-branches disappears
$k = \dfrac{\ell}{3}$	Type II	3	Nontrivial linking between the k- and the ℓ-branch disappears
$\dfrac{\ell}{3} < k < \dfrac{\ell}{\sqrt{2}}$	Type I	2	A secondary loop which connects the k- and the ℓ-branches disappears
$\dfrac{\ell}{\sqrt{2}} < k < \ell$	Type III	4	Two secondary branches switch from the ℓ-branch to the k-branch

Table 1. List of branch interactions at bifurcations points with two-dimensional kernels. In this table we make the assumption that $\lambda^* = \lambda(k, \sigma^*) = \lambda(\ell, \sigma^*)$ for some $1 \leq k < \ell$. The last column describes what happens as σ increases through σ^*.

corresponds to the secondary supercritical branches on the k-branch. The specific solutions for these cases are given again by the formulas in (22) and (23) to leading order. This completes the proof of the theorem. ☐

A brief overview of the three types of interactions with the associated ranges for the integer k is given in Table 1. From a local perspective these interactions give a complete description of how the well-known bifurcation diagram for the Cahn-Hilliard equation changes as σ increases from zero. In particular, these results show that bifurcating branches corresponding to low mode numbers eventually disappear. This has direct implications on how the trivial solution $u \equiv \mu = 0$ becomes unstable. While in the Cahn-Hilliard case the trivial solution always loses its stability to the 1-mode solution, in the diblock copolymer model the stability can be transferred to any k-mode solution. The details are collected in the following simple lemma which is stated for later reference, and whose straightforward proof is omitted.

Lemma 2 (Stability Transfer from the Trivial Solution)**.** *Consider the nonlinear elliptic problem (5) for $u \in X_\mu$ as in (6), and assume that $\mu = 0$ and $f(u) = u - u^3$, i.e., we have $f'(\mu) = 1$. For arbitrary $\sigma \geq 0$ define the positive integer $k_{\text{stab}}(\sigma)$ by*

$$k_{\text{stab}}(\sigma) = m \quad \text{for all} \quad \frac{\kappa_{m-1}\kappa_m}{\kappa_{m-1} + \kappa_m} \leq \sigma < \frac{\kappa_m \kappa_{m+1}}{\kappa_m + \kappa_{m+1}} , \quad \text{for } m \in \mathbb{N} , \tag{28}$$

where we use again the definition $\kappa_k = k^2\pi^2$. Then for fixed $\sigma \geq 0$, as λ increases from zero, the trivial solution $u = 0$ loses its stability to the nontrivial solutions on the $k_{\text{stab}}(\sigma)$-branch when

$$\lambda > \lambda_{\text{stab}}(\sigma) = \frac{\kappa^2_{k_{\text{stab}}(\sigma)}}{\kappa_{k_{\text{stab}}(\sigma)} - \sigma} . \tag{29}$$

For $\lambda \leq \lambda_{\text{stab}}(\sigma)$ the trivial solution is stable. Moreover, the function $\lambda_{\text{stab}}(\cdot)$ is continuous on $\mathbb{R}_0^+$, even though $k_{\text{stab}}(\cdot)$ obviously is not.

We close this section with a brief statement concerning symmetry connections between different solution branches. Due to the choice of boundary conditions, if an equilibrium solution is extended to a larger interval by successive even reflections at the boundary, and if the so-extended solution is then rescaled to the interval $(0,1)$, the resulting function is again an equilibrium solution for the diblock copolymer equation, yet for different values of the parameters λ and σ. More precisely, one can show that an m-fold reflection followed by the compression $x \mapsto x/m$ of an equilibrium u for the parameters (λ, σ), results in a new equilibrium at the parameter pair $(m^2\lambda, m^2\sigma)$.

3. Numerical methodology.

There are three primary numerical methods used in this work: direct simulation, numerical continuation in one and two parameters, and stability computations for equilibrium solutions. Direct simulations are used to compute the typical behavior of solutions at a variety of parameter values. Numerical continuation is then used to elucidate the results of direct simulations, in combination with the theoretical results from the last section. One-parameter continuation is used to compute the bifurcation structure of the problem with respect to the parameter λ. This choice is due to the fact that $\sigma = 0$ yields the Cahn-Hilliard equation, for which the bifurcation structure with respect to λ is known analytically. Thus our approach is to look at how the bifurcation diagram with respect to λ varies as σ increases from zero. A stability computation is performed at each equilibrium point computed. Numerical continuation in two parameters is used to follow the location of specific bifurcations observed in the one parameter case in the (σ, λ) plane. This allows us to easily locate bifurcation points as they move further from the known equilibrium.

3.1. Spectral discretization.

All of these numerical methods require a discretization of the underlying partial differential equation. This discretization is done using a spatial spectral method. Specifically, it is natural to use a discretization using Fourier series, since the only differential operator in the equation is the Laplacian, whose eigenfunctions on the domain $\Omega = (0,1)$ subject to Neumann boundary conditions are given by $\cos(k\pi x)$ for $k \in \mathbb{N}_0$. It is well known that the Fourier cosine series expansion of a smooth solution to our partial differential equation will exhibit exponentially fast convergence in the number of involved series terms. In other words,

$$u(x) = \sum_{k=0}^{\infty} a_k \cos(k\pi x) \approx \sum_{k=0}^{N} a_k \cos(k\pi x)$$

for relatively small values of N. In most of this work we have found that $N = 60$ is sufficient to see little variation in the approximations when we increase the number of involved terms. That is, the coefficients of the modes whose frequency is near N are very small relative to the others, and the modes of even higher frequency are generally even smaller and thus can be reasonably discarded. Our computations have shown that the resulting errors are less than 10^{-6} when measured in the maximum norm of the solutions.

Much of the computational aspect of the problem is simplified by using this discretization. In particular, the operation of computing the second derivative reduces to multiplying the vector of Fourier coefficients by a diagonal matrix, since the entries of this vector are coefficients of the cosines. That is, if we have

$$u = \sum_{k=0}^{N} a_k \cos(k\pi x) , \qquad \text{then} \qquad u'' = -\sum_{k=1}^{N} k^2\pi^2 a_k \cos(k\pi x) ,$$

and so the coefficients a_k are each multiplied by $-k^2\pi^2$. The discretization does not need to be as fine as, for example, a finite difference method. However, the operation of computing the nonlinearity is made more complicated, because there is no simple function relating the Fourier coefficients of a function to the Fourier coefficients of the third power of that function. However, a Galerkin method can be used to compute the nonlinearity. By computing at least $3N$ function values, the Fourier coefficients of this particular nonlinearity can be computed exactly. This is due to the identity

$$\begin{aligned} u^3 &= \left(\sum_{k=0}^{N} a_k \cos(k\pi x)\right)^3 = \sum_{i=0}^{N}\sum_{j=0}^{N}\sum_{k=0}^{N} a_i a_j a_k \cos(i\pi x)\cos(j\pi x)\cos(k\pi x) \\ &= \sum_{i,j,k=0}^{N} \frac{a_i a_j a_k}{4}\left(\cos((i-j-k)\pi x) + \cos((i+j-k)\pi x)\right. \\ &\qquad\qquad \left. + \cos((i-j+k)\pi x) + \cos((i+j+k)\pi x)\right) , \end{aligned}$$

which shows that the highest frequency term in this sum is the $\cos(3N\pi x)$-term. In practice the vector of Fourier coefficients is then truncated back to length N, resulting in a good approximation of the nonlinearity. Computationally speaking, the Fourier transforms necessary to do this analysis were performed by FFTW's discrete cosine transform in this work, which can be called directly either from the direct simulation code or from the user-provided function file in AUTO.

3.2. Direct simulation.

Direct simulation is used in combination with numerical continuation in this work. The two methods complement each other closely. For example, numerical continuation may find that there are multiple globally stable equilibria for a given parameter value. Without direct simulation, information about attraction to the different equilibria from different initial conditions is not available. It is even possible that the basins of attraction of some stable equilibria may not contain the initial conditions of interest, which in our context are random, small perturbations from the homogeneous equilibrium. Note that such initial conditions simulate a state which is almost perfectly mixed; such a state would be typical of a diblock copolymer melt before separation.

On the other hand, direct simulation also misses certain information. One such example is metastability, during which a given state may appear to be stable in the simulation, whereas this apparent stability is only due to the fact that the time frame for further evolution is too long to be captured numerically. Using direct simulation alone, an incorrect conclusion could be drawn. It is also possible for motion to be so slow in the continuous case that it does not even appear in the discretized equation until the discretization becomes much more fine, or in some cases infinitely fine. Numerical continuation can often resolve metastability issues; since normally a metastable state would be near an equilibrium point, stability computation at that equilibrium would show that it was weakly unstable. For more details on this phenomenon in the context of the related Cahn-Hilliard model we refer the reader to [5, 10].

For our direct simulations of the diblock copolymer equation we combine the above-mentioned spectral spatial discretization with a linearly implicit time-stepping algorithm. The scheme used was developed for the diblock copolymer model in [1], and is based on related methods which were discussed in [10, 11, 15].

In compact notation, this scheme is defined by

$$\hat{u}_j^{(k+1)} = \frac{\hat{u}_j^{(k)} + h\lambda \widehat{(u-u^3)}_j^{(k)} K_j}{1 + hK_j^2 + h\lambda\sigma} ,$$

where the subscripts $j = 1, 2, \ldots, N$ index vectors, superscripts denote temporal iterates, hats denote vectors of Fourier coefficients. Furthermore, K is a vector which contains the eigenvalues of the Laplacian subject to homogeneous Neumann boundary conditions, and h is the step size for the time-stepping. For more details we refer the reader to [1, 10, 11, 15]. The size N of the spectral discretization is again generally chosen to be 60, and h is on the order of 10^{-6} or 10^{-7}. The primary reason for the choice of h is due to the fact that the observed motion of the solution is quite fast early on in a simulation. A dynamic step size could significantly improve the method, but this was not necessary for our studies.

All direct simulations in this paper were performed from small random perturbations of the homogeneous equilibrium. Perturbations were applied to each of the 60 modes using a uniform distribution between -10^{-4} and 10^{-4} for each mode; as a consequence the initial conditions are smooth but oscillatory with high frequency and low amplitude.

3.3. **Equilibrium continuation.** As mentioned before, while direct simulations are essential for understanding the transient solution behavior, long-term dynamics and issues of metastability can only be determined by developing an understanding for the equilibrium structure of the diblock copolymer equation. It is well known that the diblock copolymer model is dissipative, see for example [21]. In fact, it is a gradient system with respect to the energy defined in the introduction. Moreover, one can show that the model exhibits a global attractor, which consists of equilibrium solutions and the heteroclinic connections between them. It is therefore not surprising that a detailed study of the dynamic behavior of the model has to include a study of its equilibrium set.

For the purposes of this paper we make use of numerical continuation methods, which track equilibrium solutions in parameter dependent systems. Of particular interest for our studies is the fact that the diblock copolymer model reduces to the Cahn-Hilliard model for $\sigma = 0$, and for the latter model the complete equilibrium structure is known [14]. Starting at these known equilibria we can then determine branches of equilibrium solutions as the parameters in the system are changed continuously.

For our computations we make use of the software package AUTO [12]. This package allows for one- and two-parameter continuation, finds bifurcation points on solution branches, and enables us to follow the bifurcating branches. AUTO uses a method called pseudo-arclength continuation, which is well-suited for our applications. The discretization of the underlying diblock copolymer equilibrium problem is again based on the spectral discretization discussed in Section 3.1. One can easily see that the discretized problem furnishes the nonlinear algebraic system

$$0 = -k^4\pi^4\hat{u}_k + \lambda k^2\pi^2 \left(\widehat{u-u^3}\right)_k - \lambda\sigma\hat{u}_k \quad \text{for} \quad k = 1, \ldots, N ,$$

where $\hat{u}_1, \ldots, \hat{u}_N$ denote the Fourier coefficients of the basis functions $\cos(k\pi x)$ for $k = 1, \ldots, N$. Solving the nonlinear system in this form, however, turns out to be numerically infeasible for the parameter ranges that we are interested in. This is due to the fact that the Jacobian of the right-hand side is extremely stiff. This problem can be overcome by suitably scaling each of the individual equations in the system. While this obviously does not change the solution set of the nonlinear system, it greatly improves the condition number of its Jacobian. For our applications, we use the scaled system

$$0 = -\hat{u}_k + \frac{\lambda \left(\widehat{u - u^3}\right)_k}{k^2\pi^2} - \frac{\lambda\sigma\hat{u}_k}{k^4\pi^4} \quad \text{for} \quad k = 1, \ldots, N ,$$

and in this form solving the system is numerically feasible for the parameter ranges used in our study. Note, however, that this rescaling has implications for the stability computations which are described in more detail in the next section.

3.4. **Stability computation.** While AUTO does determine the bifurcation points along solution branches, it does so without computing the spectrum of the linearization of the nonlinear system. Bifurcation points are detected only by monitoring the sign of the determinant, and bifurcation points with an even dimensional kernel of the linearization can therefore in principle not be detected. Besides this deficiency of AUTO, information on the spectrum of the linearization of the diblock copolymer equation is also crucial for describing the precise stability of the equilibrium solutions, specifically as we increase the parameter σ from 0 and move away from the Cahn-Hilliard case, in which the stability information has been derived analytically.

For these reasons, we have implemented our own method for the computation of the index of an equilibrium solution. The index code is incorporated into our AUTO code and is performed each time an equilibrium solution is computed during the running of AUTO. For any equilibrium solution u of the diblock copolymer model its spectrum consists of an infinite sequence of real eigenvalues, which converge to $-\infty$. We are interested in the precise index, i.e., the number of positive eigenvalues for each equilibrium. For this, we begin by linearizing the diblock copolymer equation at u in the direction of a perturbation v. Every term in the equation except for $(u^3)_{xx}$ is already linear, and the latter can be linearized as $(3u^2v)_{xx}$. Thus, finding the eigenvalues of the diblock copolymer model at an equilibrium u amounts to solving the eigenvalue problem

$$-v_{xxxx} - \lambda v_{xx} + \lambda(3u^2v)_{xx} - \lambda\sigma(v - \mu) = \Lambda v ,$$

subject to homogeneous Neumann boundary conditions. In this formulation, Λ denotes an eigenvalue of the linearization. Furthermore, admissible perturbations v have to satisfy a mass constraint of zero in addition to the Neumann boundary conditions, since the diblock copolymer equation is mass conserving.

Given this setting, we need to determine a matrix representation of the linear operator on the left-hand side of the eigenvalue problem. This is accomplished again using Fourier techniques, by using the same basis functions as in the spatial discretization discussed earlier. This approach makes most of the terms in the resulting matrix straightforward to compute. The second derivative operator is simply a diagonal matrix $-K$ whose diagonal entries are given by the eigenvalues of the Laplacian, i.e., they are given by $-k^2\pi^2$ for $k = 1, \ldots, N$. Similarly, the fourth derivative is represented by the diagonal matrix K^2 whose diagonal entries are given by $k^4\pi^4$ for $k = 1, \ldots, N$. Finally, the matrix representation of the term $3u^2v$ is obtained by column-wise computation. The k-th column of this matrix consists of the Fourier coefficients of the function $3u(x)^2 \cos k\pi x$. Given the Fourier coefficients of u, this vector can be computed by a simple application of the inverse discrete Fourier transform, followed by the computation of the product in real space, and finally followed by a discrete cosine transform. Applying the matrix $-K$ then yields the matrix representation for $(3u^2 v)_{xx}$. Altogether, if we denote the matrix associated with the linear operator $v \mapsto 3u^2 v$ by $A(u)$, then the matrix representation of the linearization of the diblock copolymer equation at the equilibrium u is given by

$$J(u) = -K^2 + \lambda K - \lambda K A(u) - \lambda \sigma I \ ,$$

where I denotes the identity matrix. Eigenvalues of the matrix $J(u)$ may then be computed in order to perform the index computation, with each positive eigenvalue indicating the existence of an unstable direction. In our implementation of this stability computation is performed by first assembling the matrix $J(u)$ inside the AUTO function file, and then calling LAPACK's `dgeev` solver, also directly from the AUTO function file. Notice that while this method seems to be unnecessarily elaborate, we cannot simply enable AUTO's built in eigenvalue method, since we are working with a rescaled system — and this rescaling modifies the spectrum of the linearization.

4. **Numerical study of the long-term dynamics.** In this section we study the long-term dynamics of solutions to the one-dimensional diblock copolymer model (2) which originate close to the homogeneous equilibrium $u \equiv \mu$. We begin by providing some initial intuition through direct simulations, by randomly selecting initial conditions close to μ and following the corresponding solutions until they converge to a stable equilibrium. In this way, we are able to numerically determine a partition of the σ-λ-parameter plane with respect to the periodicity of the final limiting state. In the second part of the section we use numerical continuation techniques in combination with our theoretical results from Section 2 to provide some first insight into the observed behavior. The limiting solution behavior exhibits sharply delineated transitions between different regions, and in the third part of the section we use two-parameter continuation to track certain secondary bifurcation points in the σ-λ-plane. The resulting curves agree extremely well with the numerically computed region boundaries. This shows that the typical long-term behavior of solutions originating close to the homogeneous state is not determined by the global energy minimizer, but rather by local minimizers with considerably longer periods. In the final fourth part of the section we study the scaling properties of these curves.

4.1. **Parameter space decomposition based on long-term dynamics.** We begin our study of the long-term dynamics of the one-dimensional diblock copolymer model by numerically determining the limiting behavior of typical solutions. Since we are only interested in typical microphase separation behavior, we only consider solutions which originate close to the constant equilibrium solution μ. For the purposes of this paper we only consider the case $\mu = 0$. Starting with initial conditions which are small random perturbations of the homogeneous state $\mu = 0$, we follow their evolution until they converge to a stable equilibrium state.

Figure 5 shows typical examples of the result of using such direct simulation techniques for the parameter values $\sigma = 2$ and $\mu = 0$. Originating from a small random perturbation of the homogeneous state (shown as blue curve), the solution is followed for increasing time, and the solution shape for time $t = 0.01$ is then depicted in each of the two panels (green curve). The left panel corresponds to the parameter value $\lambda = 100$, while the right panel is for $\lambda = 260$. Notice that depending on the specific λ-value, the solution snapshot is either a 2-mode or a 3-mode solution. At the parameter value $\lambda = 100$, if one follows the solution further,

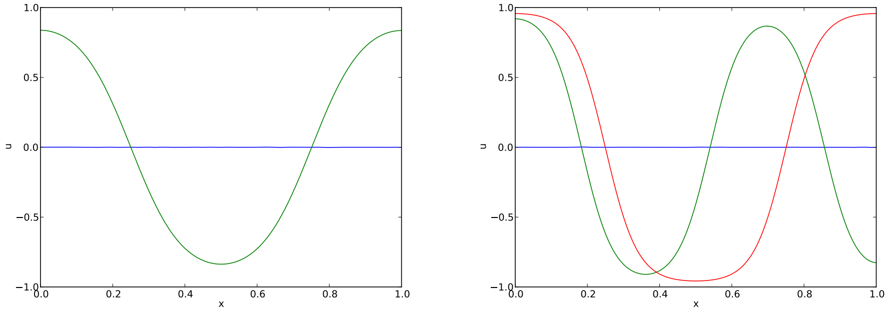

FIGURE 5. Simulation snapshots of solutions to the diblock copolymer model for $\sigma = 2$ and $\mu = 0$. The left image is for $\lambda = 100$, and shows a randomly chosen initial condition (blue curve), together with the solution at time $t = 0.01$ (green curve). For larger time, the solution profile does not change, and therefore the long-term limit appears to be an attracting 2-mode equilibrium. The right image is for $\lambda = 260$. Again in this case, the initial condition is a small perturbation of the homogeneous state (blue curve). The solution snapshot at time $t = 0.01$ is now a 3-layered function (green curve). However, the solution continues to evolve and eventually reaches a stable 2-mode solution (red curve).

the solution profile no longer changes. In other words, the green curve in the left panel of Figure 5 is close to the long-term limit. On the other hand, for $\lambda = 260$ the solution continues to change, resulting in the annihilation of one of the layers, with ultimate convergence to the attracting 2-mode solution (shown in red in the right panel). The solution behavior indicated in Figure 5 is fairly typical. Starting with a small random perturbation of the homogeneous state $\mu = 0$, solutions of the diblock copolymer equation quickly develop a periodic layered structure. Some of these layers are annihilated during the subsequent evolution, until the solution converges to a periodic stable equilibrium.

In order to obtain a more complete picture of the periodicity of the long-term dynamics of solutions originating close to the homogeneous state $\mu = 0$ we performed Monte-Carlo type simulations in a region of the first quadrant of the σ-λ-parameter plane. As indicated in the left panel of Figure 6, we subdivided this region into squares of equal size. For parameter pairs (σ, λ) which correspond to the lower left corner of these squares, we randomly chose initial conditions close to the homogeneous equilibrium and followed their evolution until convergence. The number of transition layers of the observed limits are then indicated by a coloring of the underlying square, as indicated in the color bar next to the left panel. For dark blue squares, the homogeneous state is attracting, so no phase separation takes place. The colors light blue, green, and red correspond to limits with one, two, and three transition layers. We refer to these solutions as 1-mode, 2-mode, and 3-mode solutions. Notice that in some squares, intermediate colors are observed, most notably the orange squares in the center of the left panel. In these cases the periodicity of the long-term limit was not unique, i.e., we observed multi-stability. Some of the long-term limits are shown in the right panel of Figure 6. From top left

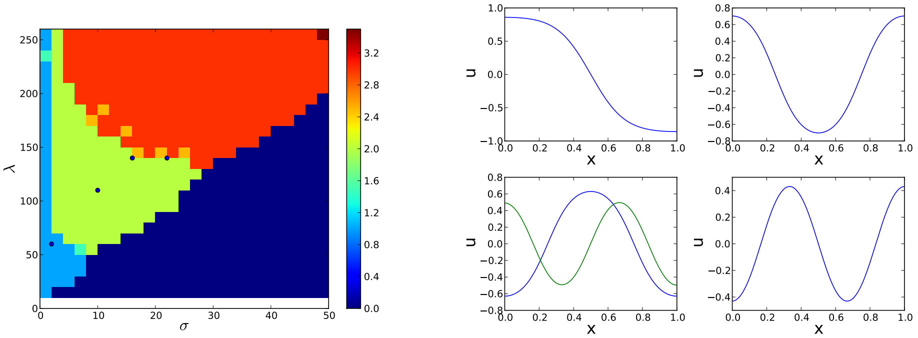

FIGURE 6. Parameter space decomposition based on the periodicity of the long-term limit. The panel on the left shows a partition of part of the σ-λ-parameter plane into squares. For the parameter values corresponding to the lower left corner of each square, direct long-term simulations were performed until the solutions reached their limiting attracting equilibrium. Colors in the image relate to the periodicity of this limit — the numbers in the color bar indicate how many layers the limit has. Dark blue squares indicate that the homogeneous state is attracting. Intermediate colors denote apparent multi-stability, i.e., different runs lead to long-term limits with different periodicities. The right panel shows some of the observed long-term limits. From top left to bottom right, the images are for the parameter values $(\sigma, \lambda) = (2, 60)$, $(10, 110)$, $(16, 140)$, and $(20, 140)$. The locations of these parameter combinations are indicated by black dots in the left panel. Note the bistability in the third of these examples.

to bottom right, the images are for the parameter values $(\sigma, \lambda) = (2, 60)$, $(10, 110)$, $(16, 140)$, and $(20, 140)$, as indicated by black dots in the left panel. Note that the third of these parameter combinations led to bistability, i.e., we observed 2-mode and 3-mode equilibria as long-term limits.

Despite the coarseness of the diagram in Figure 6, some early conclusions can be drawn. First, for fixed λ and as the parameter σ increases, lower mode equilibria become less and less stable until eventually the homogeneous equilibrium becomes globally stable. This is an immediate consequence of Lemma 2, which also shows that the boundary of the dark blue region is in fact given by the continuous function $\lambda = \lambda_{\text{stab}}(\sigma)$ defined in (29). Second, if we keep $\sigma > 0$ fixed and increase λ, then the number of transition layers in the limiting equilibrium increase by one at discrete values of the parameter λ. While there are signs of multi-stability, these seem to be confined to a fairly narrow region around well-defined smooth curves in the σ-λ-parameter plane. In the remainder of this section we describe these curves in more detail.

4.2. **One parameter bifurcation diagrams.** In this section we use the numerical continuation techniques described in Section 3.3 to understand the equilibrium structure of the diblock copolymer model for fixed σ. Specifically, we use the continuation software AUTO [12] to compute one parameter bifurcation diagrams with bifurcation parameter $\lambda > 0$. Four such diagrams were already shown in Figure 1

Equilibrium Index Color Legend						
Index	0	1	2	3	4	5
Color	Black	Red	Blue	Green	Magenta	Cyan

Table 2. Color legend for the index information shown in the bifurcation diagrams.

in Section 2. The figure contains the bifurcation diagrams for the classical Cahn-Hilliard model, i.e., for $\sigma = 0$, and the diblock copolymer bifurcation diagram for $\sigma = 6$. Each diagram is presented in two different ways: In the left column the vertical axis shows the energy of the equilibria, while the right column uses the L^2-norm. The branches in all of these diagrams are color coded in such a way that the index of the equilibria can readily be read off. The legend used throughout this paper is contained in Table 2.

It was shown rigorously in Section 2 that as σ increases from zero, the bifurcation points on the horizontal trivial solution line move to the right. In fact, we saw that the bifurcation point associated with the kernel function $\varphi_k(x) = \sqrt{2}\cos k\pi x$ will converge to $+\infty$ and on the way interact with the ℓ-mode branches for all $\ell > k$. This is further illustrated in Figure 7. When σ is nonzero, but small enough that the interaction between the 1-mode and the 2-mode branches has not yet occurred, i.e., if $0 < \sigma < 4\pi^2/5 \approx 7.896$, the branches are still in the same order as their mode index. Near the homogeneous equilibrium, each bifurcating branch has one more unstable direction than the one before it. This can be seen in the top left panel of Figure 7, showing $\sigma = 6$. However, unlike the Cahn-Hilliard case, every nontrivial branch exhibits secondary bifurcation points. This allows both 2-mode and 3-mode equilibria to be stable at $\sigma = 6$ for sufficiently large values of λ.

As σ increases past $4\pi^2/5$ and towards $\pi^2 \approx 9.8696$, infinitely many branch interactions occur, with each of the ℓ-branches for $\ell \geq 3$. These local interactions result in meaningful changes in the stability and dynamics. As the 1-mode branch approaches the ℓ-mode branch, the first secondary bifurcation point on the ℓ-mode branch moves towards the homogeneous equilibrium, leading to the three types of local branch interactions which were rigorously described in Section 2. It can be seen from the remaining panels in Figure 7 that these local interactions affect the indices of the stationary solutions on the involved branches. The top right panel shows the situation for $\sigma = 8$. The first bifurcating branch is the 2-mode branch, which is now stable — due to the local interaction between the 1- and 2-mode branches at $\sigma = 4\pi^2/5$. The 1-mode branch bifurcates with solutions of index 1. The lower left panel in Figure 7 shows the situation after the local interactions between the 1- and 3-mode branches, which occurred at $9\pi^2/10 \approx 8.883$. For $\sigma = 9$, the first two bifurcating branches are the 2-mode and the 3-mode branches, and the 1-mode branch bifurcates with solutions of index 2. Finally, the lower right panel is for $\sigma = 9.5$, which is after the 1-mode branch has interacted with the 5-mode branch, but before it crosses the 6-mode branch. The 1-mode branch now contains equilibria of index 4. As σ increases towards π^2, the 1-mode branch converges to $+\infty$.

The pattern described above then repeats for each of the remaining branches. First the 2-mode branch interacts with the ℓ-mode branches for $\ell \geq 3$, until it eventually disappears to infinity at $\sigma = 4\pi^2$, and so on. As this proceeds, the higher mode branches gradually become more and more stable, until eventually

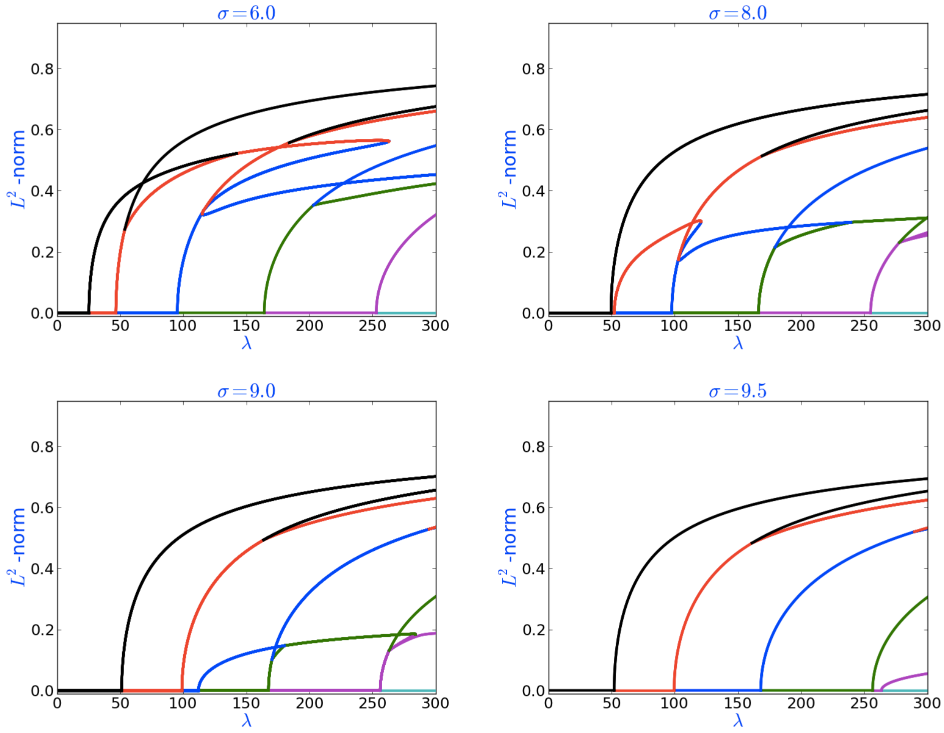

FIGURE 7. Bifurcation diagram changes with increasing σ. For $\sigma = 6$ part of the 1-mode branch is still stable, as indicated by the color black. As σ increases to $\sigma = 8$, the 1-mode branch moves to the right and interacts with the 2-mode branch. For $\sigma = 8$, the 2-mode branch is now the leftmost branch, and it has inherited the stability from the 1-mode branch. The latter bifurcates from the trivial solution now as an index 1 branch, as indicated in red. As σ increases further, the 1-mode branch moves further to the right. For $\sigma = 9$ it bifurcates between the 3-mode and 4-mode branches and contains equilibria of index 3, and for $\sigma = 9.5$ it bifurcates to the right of the 5-mode branch and contains index 5 equilibria. Colors indicate the stability properties on the equilibrium solutions, according to Table 2.

when the $(\ell - 1)$-mode branch crosses the ℓ-mode branch, at which point the ℓ-mode branch becomes stable. It should not come as a surprise that these latter stability-inducing interactions are of central importance. They are studied in more detail in the next section.

We close this section by demonstrating how the information of the bifurcation diagrams relates to the direct solution simulations in Section 4.1. For this, consider the two bifurcation diagrams in Figure 8, which are for $\sigma = 2$ and $\mu = 0$. Both diagrams depict the same equilibrium solutions, but in the left panel the energy is used on the vertical axis, while in the right panel we use again the L^2-norm. In Figure 5 of the previous section, we presented solution snapshots of two diblock copolymer solutions which originate close to the homogeneous state $\mu = 0$. The

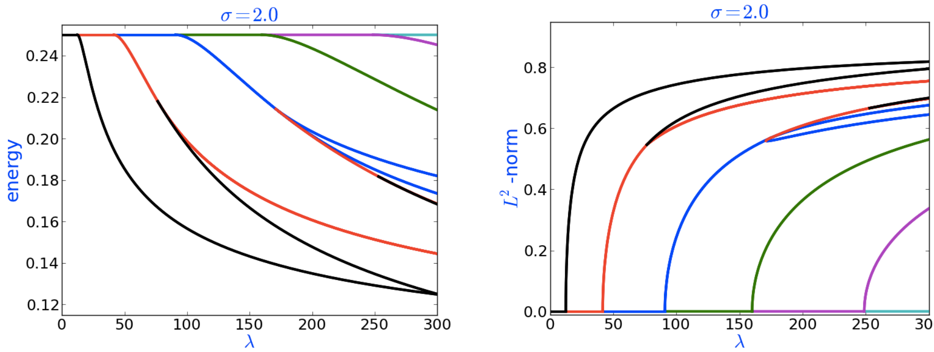

FIGURE 8. Bifurcation diagrams for $\sigma = 2$ and $\mu = 0$. In the left diagram, the value of the equilibrium energy is used on the vertical axis, while in the right diagram the L^2-norm is used. Colors indicate the stability properties of the equilibrium solutions, according to Table 2.

first of these is for $\lambda = 100$, and the solution converges to the 2-mode equilibrium as $t \to \infty$. It is evident from the bifurcation diagrams in Figure 8 that the 2-mode stationary solution is an attracting solution with index 0. In fact, the 2-mode solutions gain stability at a secondary bifurcation point at $\lambda \approx 76.5973$. Note, however, that the attracting 2-mode equilibrium is not the global energy minimizer for $\lambda = 100$. The left panel in Figure 8 shows that the energy of the 1-mode solution is in fact lower. In other words, the dynamics leads the solution to a local energy minimizer, rather than the global minimizer.

In contrast, we now reconsider the solution snapshots shown in the right panel of Figure 5, where $\lambda = 260$. In this case we have seen that while the solution seems to approach the 3-mode equilibrium, it eventually converges to the 2-mode equilibrium. As it turns out, for $\lambda = 260$ the ℓ-mode equilibria for $\ell = 1, 2, 3$ are all attracting, since the stability-inducing secondary bifurcation on the 3-mode branch occurs at $\lambda \approx 253.079$. In other words, even though the 3-mode equilibrium is attracting, the evolution only takes the solution close to the associated domain of attraction, rather than into it.

We would like to close this section by demonstrating that the diblock copolymer evolution can lead solutions close to equilibrium solutions, even if they are unstable. The left panel of Figure 9 shows snapshots of a solution which originates close to the homogeneous state, for $\lambda = 56$, $\sigma = 5$, and $\mu = 0$. The evolution takes the solution close to the 2-mode equilibrium, before the apparent symmetry of the solution is broken and it converges to the stable 1-mode equilibrium. In the right panel of Figure 9 one can see the associated bifurcation diagram for $\sigma = 5$ and $\mu = 0$. The solutions on the 2-mode branch become stable at $\lambda \approx 56.77$, i.e., for $\lambda = 56$ the 2-mode equilibrium has still index 1. Nevertheless, the dynamic evolution "senses" the fact that this state is close to stability, and therefore remains close to it for a fairly long time. This phenomenon is often referred to as intermittency.

4.3. **Stability region boundaries and two-parameter continuation.**

The results of the previous two sections have provided us, among other things, with the

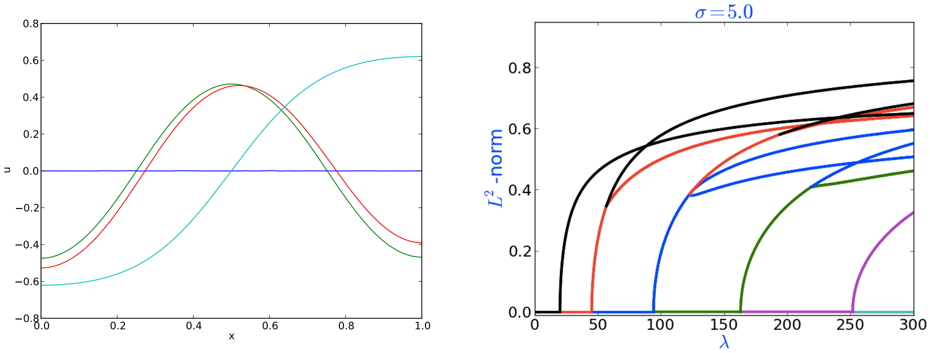

FIGURE 9. The left panel contains simulation snapshots for $\lambda = 56$, $\sigma = 5$, and $\mu = 0$. The initial condition is shown in blue, the green curve shows the state at time $t = 0.1$, and the red curve is for $t = 0.3$. In both cases, the solution qualitatively has the shape of the 2-mode equilibrium, albeit with broken symmetry. The long-term limit is shown in cyan, and is reached after about $t = 0.4$. The panel on the right shows the bifurcation diagram for $\sigma = 5$. The secondary bifurcation point on the 2-mode branch occurs at $\lambda \approx 56.77$, i.e., the 2-mode equilibrium is still unstable with index 1 for $\lambda = 56$.

following crucial insights. If the first branch bifurcating from the trivial solution line is the $(k-1)$-mode branch for some $k \geq 2$, then the solutions appearing on this nontrivial branch exhibit the same periodicity as the kernel function $\varphi_{k-1}(x) = \sqrt{2}\cos((k-1)\pi x)$. As σ increases, the $(k-1)$-branch moves to the right until it interacts with the k-branch along the homogeneous equilibrium. Note that solutions on the k-branch have the same periodicity as the kernel function $\varphi_k(x) = \sqrt{2}\cos(k\pi x)$. Before the branch interaction, the $(k-1)$-branch is stable near the homogeneous equilibrium, and the k-branch is unstable with index 1 near the homogeneous equilibrium. In addition, our rigorous local analysis from Section 2 shows that for σ below and near the interaction, there exists a secondary bifurcation point on the k-branch beyond which solutions are attracting (index 0). Immediately after the bifurcation where the $(k-1)$-mode branch interacts with the k-mode branch, the solutions on the k-branch are all attracting. Near the homogeneous equilibrium, solutions on the k-branch remain attracting until the k- and $(k+1)$-branches interact. In particular, the secondary bifurcation point is no longer present on the k-mode branch after the local branch interaction, as it has converged to the trivial line. However, our rigorous results are local and thus do not rule out the possibility of secondary bifurcations for σ values far from both the bifurcation and the homogeneous equilibrium.

The situation described in the above paragraph can be seen for $k = 2$ in Figure 7. In particular, for $\sigma = 6.0$ the system is prior to bifurcation. The 1-branch is the leftmost branch, and the 2-branch is immediately to the right of it. Near the homogeneous equilibrium, all solutions on the 1-branch are stable (black) and all solutions on the 2-branch are index 1 (red). Away from the trivial line, there is a secondary bifurcation to stable solutions on the 2-branch. This secondary bifurcation can also be seen at $\sigma = 5$ and $\lambda \approx 56.77$ as shown in the righthand image of Figure 9. The system is shown after the bifurcation at $\sigma = 8.0, 9.0, 9.5$. The 2-branch is the leftmost branch — consisting of stable solutions, and the 1-branch is immediately to the right of it — consisting of index 1 solutions near the homogeneous equilibrium.

We have seen using direct simulation that when λ exceeds the λ-value of the stabilizing secondary bifurcation point described above, the newly stabilized branch is often reached by solutions originating close to the homogeneous state in the long term, even if other stable solutions exist. In fact, we have seen cases where the stable solutions on the k-mode are the long-term limit of solutions starting near the homogeneous state, even though they are not global energy minimizers. Thus the stabilizing secondary bifurcation point is central to our understanding of the dynamics of the diblock copolymer equation, as we emphasize with the following definition.

Definition 4.1 (Stabilizing Secondary Bifurcation Point)**.** Assume that $\mu = 0$, and let $k \geq 2$ be an integer. It was shown rigorously in Theorems 2.2 and 2.4 that for σ-values right before the local interaction between the $(k-1)$-branch and the k-branch, there exists a secondary bifurcation point on the k-branch, which converges to the trivial solution as σ approaches $\kappa_{k-1}\kappa_k/(\kappa_{k-1}+\kappa_k)$. This point is called a *stabilizing secondary bifurcation point on the k-mode branch*, and it exists at least locally on a smooth curve for $\sigma < \kappa_{k-1}\kappa_k/(\kappa_{k-1}+\kappa_k)$. The corresponding local interaction between the $(k-1)$-branch and the k-branch is of Type I for $k = 2, 3$, and of Type III for $k \geq 4$.

The stabilizing secondary bifurcation points can easily be seen in the local bifurcation pictures in Section 2. For the case of a Type I interaction, i.e., for $k = 2, 3$, the $(k-1)$-mode branch is shown in blue in Figure 2, the k-mode branch is shown in red, and the stabilizing secondary bifurcation point is the point at which the red and green branches connect. For the case of a Type III interaction, i.e., for $k \geq 4$, the analogous statement applies to Figure 4.

As we mentioned earlier, numerical evidence from the last section points towards the significance of the stabilizing secondary bifurcation points with respect to the long-term dynamics of solutions originating close to the homogeneous equilibrium. Therefore, we used two-parameter continuation in AUTO to numerically determine the location of these points in the σ-λ-plane. The results of these computations are shown in Figure 10 for the case $\mu = 0$. In the left panel, the blue, green, red, cyan, and magenta curves correspond to the stabilizing secondary bifurcation points on the 2-, 3-, 4-, 5-, and 6-mode branch, respectively. These curves were determined as follows. For each of the mode numbers $k = 2, \ldots, 6$ we considered a fixed σ slightly less than $\kappa_{k-1}\kappa_k/(\kappa_{k-1}+\kappa_k)$, i.e., slightly to the left of each cusp in the figure. (The leftward offset of σ results in the appearance of a slight gap between the analytical curve (yellow) and the numerically computed curves in Figure 10, when in fact these curves are connected.) Then the stabilizing bifurcation point exists, but is still close to the homogeneous equilibrium, making it easy to obtain by regular one parameter continuation. This bifurcation point is continued in two parameters in the direction of decreasing σ, using AUTO's built in method. The yellow lower boundary curve in Figure 10 is the graph of the function $\lambda = \lambda_{\mathrm{stab}}(\sigma)$ defined in (29). Recall that this curve has been analytically determined, and it delineates the region in which the homogeneous state is stable from the region of

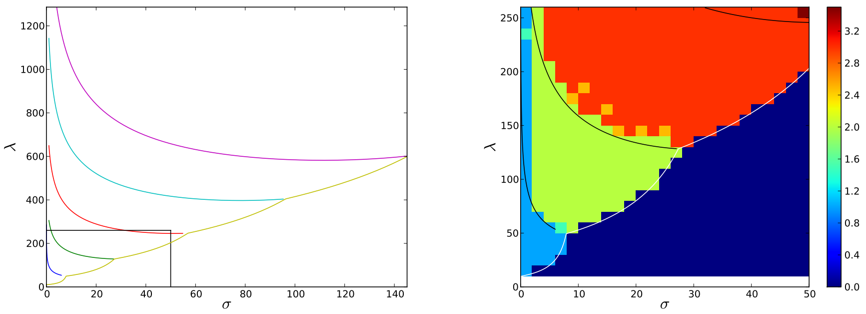

FIGURE 10. The left panel shows a bifurcation theoretic parameter space decomposition based on the stabilizing secondary bifurcation points introduced in Definition 4.1. The blue, green, red, cyan, and magenta curves correspond to the stabilizing secondary bifurcation points on the 2-, 3-, 4-, 5-, and 6-mode branch, respectively, obtained via two-parameter continuation. The yellow lower boundary curve is the graph of the function $\lambda = \lambda_{\text{stab}}(\sigma)$ defined in (29). All computations were performed for total mass $\mu = 0$. For the region indicated by black lines in the left image, the right panel shows an overlay of the diagram from Figure 6 with the curves of the left panel. Since the direct simulations were performed for the parameter values at the bottom left corner of each square, the location curves of the stabilizing secondary bifurcation points seem to delineate the regions found in Figure 6.

its instability. The cusps in the curve are the points at which the mode number k changes as in (28). In the right panel of Figure 10 these smooth location curves are finally superimposed onto the numerically obtained parameter space partition from Figure 6. The panels in this figure give a surprisingly clear picture of the long-term dynamics of the diblock copolymer model, with smooth separations between the regions of different long-term periodicity. This is particularly surprising since the curves shown in the left panel arise from local stability changes, while the direct simulation partition in the right panel addresses the global, long-term dynamics.

In order to determine in more detail how well the location curves based on two-parameter continuation delineate the regions with different long-term behavior, we performed another set of direct simulations, which are now based on the results from the bifurcation study. These continuation-informed simulation diagrams are shown in Figures 11 and 12. For this, we performed direct simulations of solutions to the diblock copolymer model which originate close to the homogeneous equilibrium, but for parameter combinations (σ, λ) chosen from a small neighborhood of the location curves from Figure 10. Each dot in Figure 11 corresponds to one considered parameter combination, and the color of the dot represents the observed periodicity of the long-term limit, corresponding to the color bar on the right. Blowups of the behavior close to each of the four location curves are shown in Figure 12.

While it is intuitive to perform simulations at points near the suspected stability boundaries, the nearby points must be chosen in some way. A natural albeit simple way to do this is to go out from the stability boundaries along perpendicular lines.

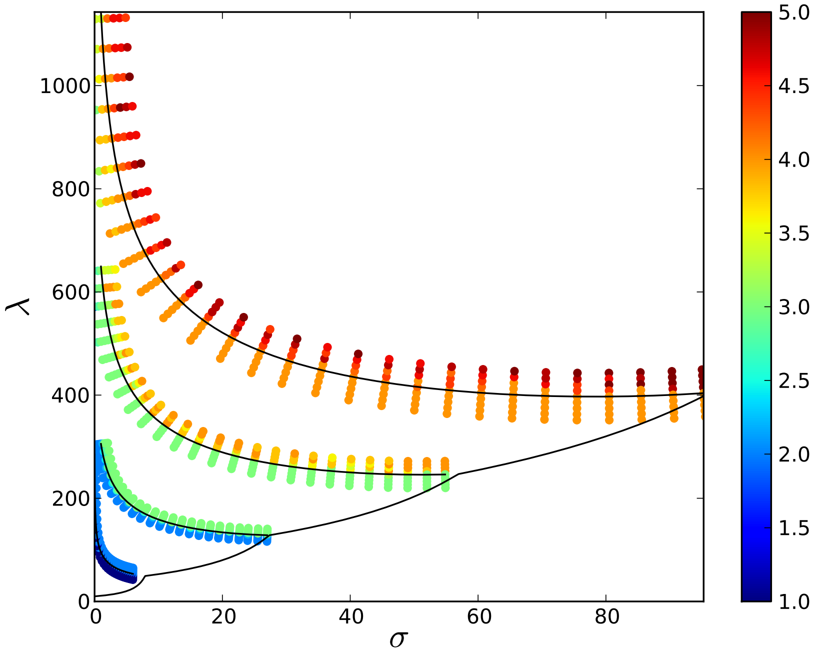

Figure 11. The full continuation-informed simulation diagram. Colors correspond to indices as in Figure 6. The overall trend is that above each curve we see a new index to a significant extent; the strength of this effect appears to decrease somewhat as λ increases. For comparison, the location curves of the stabilizing secondary bifurcations from the left panel of Figure 10 are also shown.

In generating Figures 11 and 12, our notion of "perpendicular" is in a modified coordinate system where σ and λ are on the same scale, so that the lines actually appear perpendicular in the figure. That is, if $(T_\sigma, T_\lambda) \in \mathbb{R}^2$ is the tangent to the location curve at a given point, then the "perpendicular direction" $(P_\sigma, P_\lambda) \in \mathbb{R}^2$ satisfies the identity

$$\frac{P_\sigma T_\sigma}{\sigma_{\max,k}} + \frac{P_\lambda T_\lambda}{\lambda_{\max,k}} = 0 \,,$$

where $\sigma_{\max,k}$ and $\lambda_{\max,k}$ are the maximal considered values of σ and λ, respectively, for the location curve of the stabilizing secondary bifurcation points on the k-mode branch as shown in Figure 12.

The overall result of these simulations is that the location curves of the stabilizing secondary bifurcation points are indeed central to understanding the long-term dynamics of the diblock copolymer equation, at least in the context of solutions originating close to the homogeneous equilibrium. In general, slightly below a k-mode location curve, we see long-term limits with the same periodicity as the $(k-1)$-mode equilibrium, and occasionally lower periodicities as well. Slightly above the location curve of the stabilizing secondary bifurcation points on the k-mode branch we tend to see a mix of $(k-1)$-mode and k-mode long-term limits, but as the distance from the location curve increases the k-mode equilibria begin to dominate the long-term behavior. For the case $k = 2$, which was discussed in Section 4.1, the newly

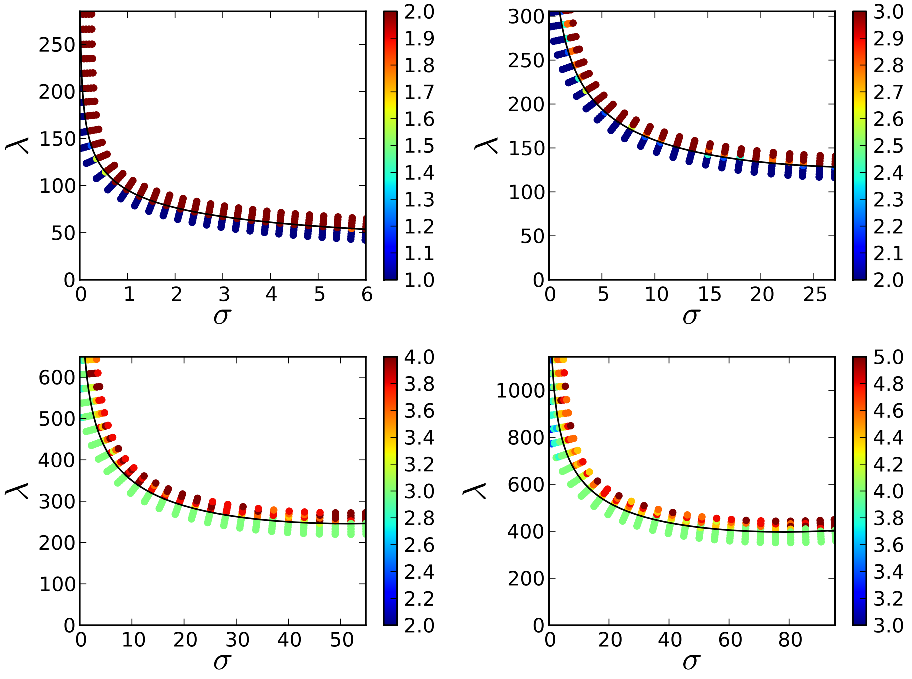

FIGURE 12. The individual continuation-informed simulation diagrams. These correspond to the location curves of the stabilizing secondary bifurcations on the k-mode branches for $k = 2, 3, 4, 5$, from top left to bottom right. Notice that for $k = 4$ and $k = 5$ the level of multi-stability is somewhat more pronounced than for $k = 2$ and $k = 3$.

stabilized 2-mode stationary solution dominates the dynamics almost immediately. Recall also that for $k = 3$ we have seen in Figures 5 and 8 that for relatively small distances from the location curve the 2-mode solution still dominates the behavior.

We would like to point out that at first glance, Figure 12 seems to indicate that for the mode numbers $k = 4$ and $k = 5$ there are three different periodicities present on the perpendicular simulation lines. However, a closer look reveals the reason for the appearance of the third periodicity. These points are located at small σ-values and high λ-values, i.e., towards the upper left corner of the diagrams, which can clearly be seen for the case $k = 5$. Thus, due to the choice of scale used for the perpendicular lines, they actually cross the location curves of the stabilizing secondary bifurcation points for lower mode numbers, thereby leading to their appearance as long-term limits.

Overall, two-parameter continuation of the location curves of the stabilizing secondary bifurcation points introduced in Definition 4.1 seems to provide a systematic *a priori* way to determine the typical periodicity of the long-term limit of solutions of the diblock copolymer model which originate close to the homogeneous equilibrium. Moreover, while the diblock copolymer model does exhibit multi-stability in the simulations for a fixed (σ, λ)-parameter pair, the dominance of certain mode numbers is established already at fairly short distances from the location curves.

4.4. **Asymptotic analysis and scaling behavior.** In this final part of the section we discuss the scaling behavior of the location curves introduced above, as the mode number k increases to ∞. It was mentioned at the end of Section 2 that the diblock copolymer equation exhibits the following fundamental scaling property: If $m \in \mathbb{N}$ is an arbitrary positive integer, and if u denotes a stationary solution of the diblock copolymer model for the parameter combination (σ, λ) with the same periodicities as the k-mode kernel function $\varphi_k(x) = \sqrt{2} \cos k\pi x$, then an m-fold reflection followed by the compression $x \mapsto x/m$ furnishes a new equilibrium at the new parameter combination $(m^2\sigma, m^2\lambda)$ which has the same periodicities as the kernel function φ_{mk}. In other words, branches of k-mode solutions the parameter pair (σ, λ) immediately give rise to branches of mk-mode solutions at the new parameter combination $(m^2\sigma, m^2\lambda)$. Even more is true. If the function u corresponds to a bifurcation point in the bifurcation diagram for (σ, λ), then the new solution corresponds to a bifurcation point for $(m^2\sigma, m^2\lambda)$.

At first glance, the above reasoning appears to allow us to obtain detailed scaling information for the location curves of the stabilizing secondary bifurcation points on the k-mode branch, as $k \to \infty$. Unfortunately, this is not quite true. To see this, consider the branch interaction which generates the secondary bifurcation points of interest, i.e., the interaction between the $(k-1)$-mode and the k-mode branch. Using the above scaling, one can relate this interaction to the interaction between the $m(k-1)$-mode and the mk-mode branch. Yet, the stabilizing secondary bifurcations on the mk-mode branch are generated through its interaction with the $(mk-1)$-branch — and this interaction occurs in fact for a larger λ-value. In other words, the scaling can only provide a lower bound on the location curves with higher mode numbers. Despite this fact, the scaling $(\sigma, \lambda) \mapsto (m^2\sigma, m^2\lambda)$ is of importance, as the following simple lemma shows.

Lemma 3. *Consider the diblock copolymer model on the domain* $\Omega = (0, 1)$ *with* $f(u) = u - u^3$ *and assume that the total mass* μ *satisfies* $f'(\mu) > 0$. *For any mode number* $k \geq 2$, *consider the parameter combination*

$$\sigma_k^* = \frac{f'(\mu)\kappa_{k-1}\kappa_k}{\kappa_{k-1} + \kappa_k} \qquad \text{and} \qquad \lambda_k^* = \frac{\kappa_k^2}{f'(\mu)\kappa_k - \sigma_k^*} = \frac{\kappa_{k-1} + \kappa_k}{f'(\mu)}$$

at which the $(k-1)$*-mode branch interacts with the* k*-mode branch as described in Section 2. Then we have*

$$\lim_{k\to\infty} \left(\frac{\sigma_k^*}{k^2}, \frac{\lambda_k^*}{k^2} \right) = \left(\frac{f'(\mu)\pi^2}{2}, \frac{2\pi^2}{f'(\mu)} \right) .$$

In other words, after division by k^2 *the lower right endpoints of the location curves of the stabilizing secondary bifurcation points on the* k*-mode branch converge.*

Proof. The proof follows immediately from the fact that $\kappa_m = m^2\pi^2$ in our situation. □

Since the lower right endpoints of the location curves of the stabilizing secondary bifurcation points on the k-mode branch converge after rescaling by $1/k^2$, it is natural to wonder whether the location curves as a whole converge as well. In the left panel, the rescaled curves are shown in blue, green, red, cyan, and magenta for $k = 2, 3, 4, 5, 6$, respectively.[1]. This diagram clearly indicates that the curves seem

---

[1] According to the above Lemma 3, the lower right endpoints of the rescaled location curves will converge to the point $(\ln(\pi^2/2), \ln(2\pi^2)) \approx (1.596, 2.983)$. The discrepancy apparent in Figure 13

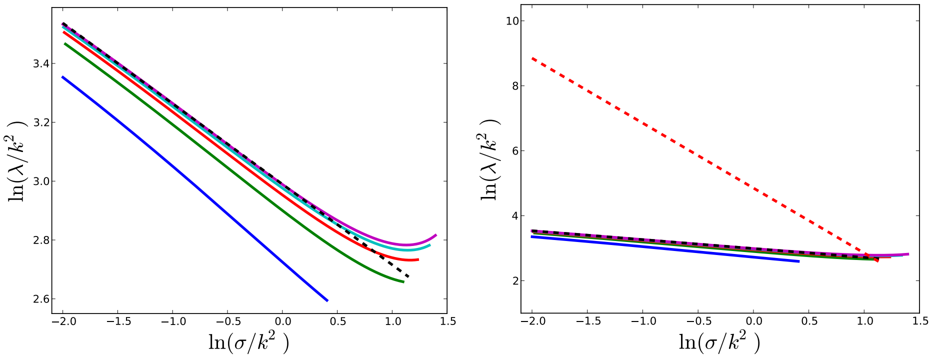

FIGURE 13. Scaled versions of the location curves of the stabilizing secondary bifurcation points on the k-mode branch, as introduced in Definition 4.1. The left panel shows these location curves scaled by $1/k^2$ in both the σ- and the λ-direction in a log-log plot. The curve corresponding to mode number $k = 2, 3, 4, 5, 6$ is shown in blue, green, red, cyan, magenta, respectively. The dashed black curve is a least squares fit of the visible linear behavior. The right panel contains all the curves shown on the left, but in addition also the rescaled curve at which the k-mode solution becomes the global energy minimizer. The latter curve is shown as dashed red line.

to converge to a universal limit. In fact, since we chose logarithmic units on both axes, the figure implies that after the rescaling the location curves satisfy a power law. Using a least squares fit, which ignores the transient behavior on the lower right ends of the curves, this furnishes the following relation:

- Stabilizing secondary bifurcation point on k-mode branch:

$$\frac{\lambda}{k^2} \approx 19.88 \cdot \left(\frac{\sigma}{k^2} \right)^{-0.2738} . \tag{30}$$

This formula provides an asymptotic estimate as to when the stable k-mode equilibrium can be expected to be the long-term limit of solutions of the diblock copolymer equations which originate close to the homogeneous equilibrium. But what does this limiting periodicity have to do with the periodicity of the global energy minimizer? In other words, is there an asymptotic formula for when the k-mode equilibrium becomes the global energy minimizer? As was stated in the introduction, asymptotically this happens when λ, σ, and k satisfy (4), and this formula clearly also respects the scaling by $1/k^2$. In fact, formula (4) can be rewritten as follows:

- Global energy minimizing k-mode equilibrium:

$$\frac{\lambda}{k^2} \approx 128 \cdot \left(\frac{\sigma}{k^2} \right)^{-2} . \tag{31}$$

This limiting curve lies considerably above the curve in (30), as shown in the right panel of Figure 13. Thus, in general the observed periodicity of the long-term limit of solutions of the diblock copolymer equations which originate close to the homogeneous equilibrium is not described by the periodicity of the global energy

---

is due to the fact that our numerically computed location curves do not start exactly at the interaction point of the $(k-1)$- and k-branches, but somewhat to the left, as discussed in the previous section.

minimizer, but rather by a local minimizer with higher periodicity. In particular, the difference in the exponents on the right-hand sides of (30) and (31) shows that the observed periodicity will in practice be considerably larger than that of the global mininizer.

5. Conclusion.

This paper is concerned with the typical long-term behavior of solutions of the diblock copolymer model on one-dimensional domains, which originate close to the homogeneous equilibrium and exhibit microphase separation. Our study is based on two different, yet complementing points of view.

First of all, by combining rigorous bifurcation theoretic results which describe the complete bifurcation structure of the equilibrium set close to the trivial solution line with numerical continuation techniques, we are able to provide insight into the global bifurcation structure. This demonstrates that even though the limit $\sigma \to 0$ reduces the diblock copolymer model to the classical Cahn-Hilliard model, the bifurcation structure of the former model is considerably more complicated. While the classical Cahn-Hilliard equation supports only two stable 1-layer equilibrium solutions, the diblock copolymer equation exhibits a wealth of stable local energy minimizers. We have described that as σ increases from zero, solution branches which were present in the Cahn-Hilliard diagram move to the right and converge to infinity, and thereby lead to an infinite sequence of branch interactions with two-dimensional bifurcation kernel. One specific type of these interactions, namely the interaction between the $(k-1)$-mode and the k-mode branch leads to the creating of stable solutions on the k-mode branch.

Secondly, we have used direct numerical simulations to determine a partition of the (σ, λ)-parameter plane into regions in which the long-term limit of the dynamics exhibits a certain periodicity. We have seen that even though multi-stability clearly does occur, the boundaries of these regions seem to be delineated by smooth parameter curves.

By combining the above two points of view, we were able to identify the delineating curves as the location curves of the stability inducing secondary bifurcation points on the k-mode branch. This was validated numerically by a new set of continuation-informed direct simulations. In addition, we obtained scaling information on the delineating curves as a function of the mode index k. This demonstrates that for the one-dimensional diblock copolymer model, the global energy minimizer does not in fact describe the typical long-term behavior of solutions originating close to the homogeneous equilibrium.

Acknowledgments. This work was partially supported by NSF-CSUMS Grant DMS-0639300 for Undergraduate Research in Computational Mathematics at George Mason University. The work of E.S. and T.W. was also partially supported by NSF grant DMS-0907818.

REFERENCES

[1] M. Atkins, “Long Term Dynamics of the Diblock Copolymer Model on Higher Dimensional Domains,” Master’s thesis, George Mason University, 2011.

[2] M. Bahiana and Y. Oono, *Cell dynamical system approach to block copolymers*, Physical Review A, **41** (1990), 6763–6771.

[3] F. Bates and G. H. Fredrickson, *Block copolymer thermodynamics: Theory and experiment*, Annual Review of Physical Chemistry, **41** (1990), 525–557.

[4] F. Bates and G. H. Fredrickson, *Block copolymers — designer soft materials*, Physics Today, **52** (1999), 32–38.

[5] D. Blömker, B. Gawron and T. Wanner, *Nucleation in the one-dimensional stochastic Cahn-Hilliard model*, Discrete and Continuous Dynamical Systems, **27** (2010), 25–52.

[6] R. Choksi, *Mathematical aspects of microphase separation of diblock copolymers*, in "Surikaisekikenkyusko Kokyuroku," Vol. 1330, RIMS, Kyoto, (2003), 10–17.

[7] R. Choksi, M. A. Peletier and J. F. Williams, *On the phase diagram for microphase separation of diblock copolymers: An approach via a nonlocal Cahn-Hilliard functional*, SIAM Journal on Applied Mathematics, **69** (2009), 1712–1738.

[8] R. Choksi and X. Ren, *On the derivation of a density functional theory for microphase separation of diblock copolymers*, Journal of Statistical Physics, **113** (2003), 151–176.

[9] D. A. Christian, A. Tian, W. G. Ellenbroek, I. Levental, K. Rajagopal, P. A. Janmey, A. J. Liu, T. Baumgart and D. E. Discher, *Spotted vesicles, striped micelles and Janus assemblies induced by ligand binding*, Nature Materials, **8** (2009), 843–849.

[10] J. P. Desi, H. Edrees, J. Price, E. Sander and T. Wanner, *The dynamics of nucleation in stochastic Cahn-Morral systems*, SIAM Journal on Applied Dynamical Systems, **10** (2011), 707–743.

[11] J. P. Desi, E. Sander and T. Wanner, *Complex transient patterns on the disk*, Discrete and Continuous Dynamical Systems, **15** (2006), 1049–1078.

[12] E. Doedel, *AUTO: A program for the automatic bifurcation analysis of autonomous systems*, Congressus Numerantium, **30** (1981), 265–284.

[13] K. Glasner and R. Choksi, *Coarsening and self-organization in dilute diblock copolymer melts and mixtures*, Physica D, **238** (2009), 1241–1255.

[14] M. Grinfeld and A. Novick-Cohen, *Counting stationary solutions of the Cahn-Hilliard equation by transversality arguments*, Proceedings of the Royal Society of Edinburgh Sect. A, **125** (1995), 351–370.

[15] T. Hartley and T. Wanner, *A semi-implicit spectral method for stochastic nonlocal phase-field models*, Discrete and Continuous Dynamical Systems, **25** (2009), 399–429.

[16] X. Kang and X. Ren, *Ring pattern solutions of a free boundary problem in diblock copolymer morphology*, Physica D, **238** (2009), 645–665.

[17] N. Q. Le, *On the convergence of the Ohta-Kawasaki equation to motion by nonlocal Mullins-Sekerka law*, SIAM Journal on Mathematical Analysis, **42** (2010), 1602–1638.

[18] S. Mahajan, S. Renker, P. Simon, J. Gutmann, A. Jain, S. Gruner, L. Fetters, G. Coates and U. Wiesner, *Synthesis and characterization of amphiphilic poly(ethylene oxide)-block-poly(hexyl methacrylate) copolymers*, Macromolecular Chemistry and Physics, **204** (2003), 1047–1055.

[19] S. Maier-Paape, K. Mischaikow and T. Wanner, *Structure of the attractor of the Cahn-Hilliard equation on a square*, International Journal of Bifurcation and Chaos, **17** (2007), 1221–1263.

[20] H. Nakazawa and T. Ohta, *Microphase separation of ABC-type triblock copolymers*, Macromolecules, **26** (1993), 5503–5511.

[21] Y. Nishiura, "Far-from-Equilibrium Dynamics," Translations of Mathematical Monographs, **209**, Iwanami Series in Modern Mathematics, American Mathematical Society, Providence, RI, 2002.

[22] Y. Nishiura and I. Ohnishi, *Rugged landscape with fine structure*, unpublished preprint.

[23] Y. Nishiura and I. Ohnishi, *Some mathematical aspects of the micro-phase separation in diblock copolymers*, Physica D, **84** (1995), 31–39.

[24] Y. Nishiura and H. Suzuki, *Higher dimensional SLEP equation and applications to morphological stability in polymer problems*, SIAM Journal on Mathematical Analysis, **36** (2004/05), 916–966.

[25] I. Ohnishi, Y. Nishiura, M. Imai and Y. Matsushita, *Analytical solutions describing the phase separation driven by a free energy functional containing a long-range interaction term*, Chaos, **9** (1999), 329–341.

[26] T. Ohta and K. Kawasaki, *Equilibrium morphology of block copolymer melts*, Macromolecules, **19** (1986), 2621–2632.

[27] X. Ren, *Shell structure as solution to a free boundary problem from block copolymer morphology*, Discrete and Continuous Dynamical Systems, **24** (2009), 979–1003.

[28] X. Ren and J. Wei, *On energy minimizers of the diblock copolymer problem*, Interfaces and Free Boundaries, **5** (2003), 193–238.

[29] X. Ren and J. Wei, *Triblock copolymer theory: Free energy, disordered phase and weak segregation*, Physica D, **178** (2003), 103–117.

[30] X. Ren and J. Wei, *Triblock copolymer theory: Ordered ABC lamellar phase*, Journal of Nonlinear Science, **13** (2003), 175–208.

[31] X. Ren and J. Wei, *Single droplet pattern in the cylindrical phase of diblock copolymer morphology*, Journal of Nonlinear Science, **17** (2007), 471–503.

[32] R. Tamate, K. Yamada, J. Vinals and T. Ohta, *Structural rheology of microphase separated diblock copolymers*, Journal of the Physical Society of Japan, **77** (2008), 034802.

[33] P. Tang, F. Qiu, H. Zhang and Y. Yang, *Morphology and phase diagram of complex block copolymers: ABC linear triblock copolymers*, Physical Review E, **69** (2004), 031803.

[34] R. Wang, J. Hu, Z. Jiang and D. Zhou, *Morphology of ABCD tetrablock copolymers predicted by self-consistent field theory*, Macromolecular Theory and Simulations, **14** (2005), 256–266.

[35] E. Zeidler, "Nonlinear Functional Analysis and its Applications. I. Fixed-Point Theorems," Springer-Verlag, New York, 1986.

Received May 2012; revised November 2012.

E-mail address: `ijohnso1@masonlive.gmu.edu`
E-mail address: `esander@gmu.edu`
E-mail address: `twanner@gmu.edu`